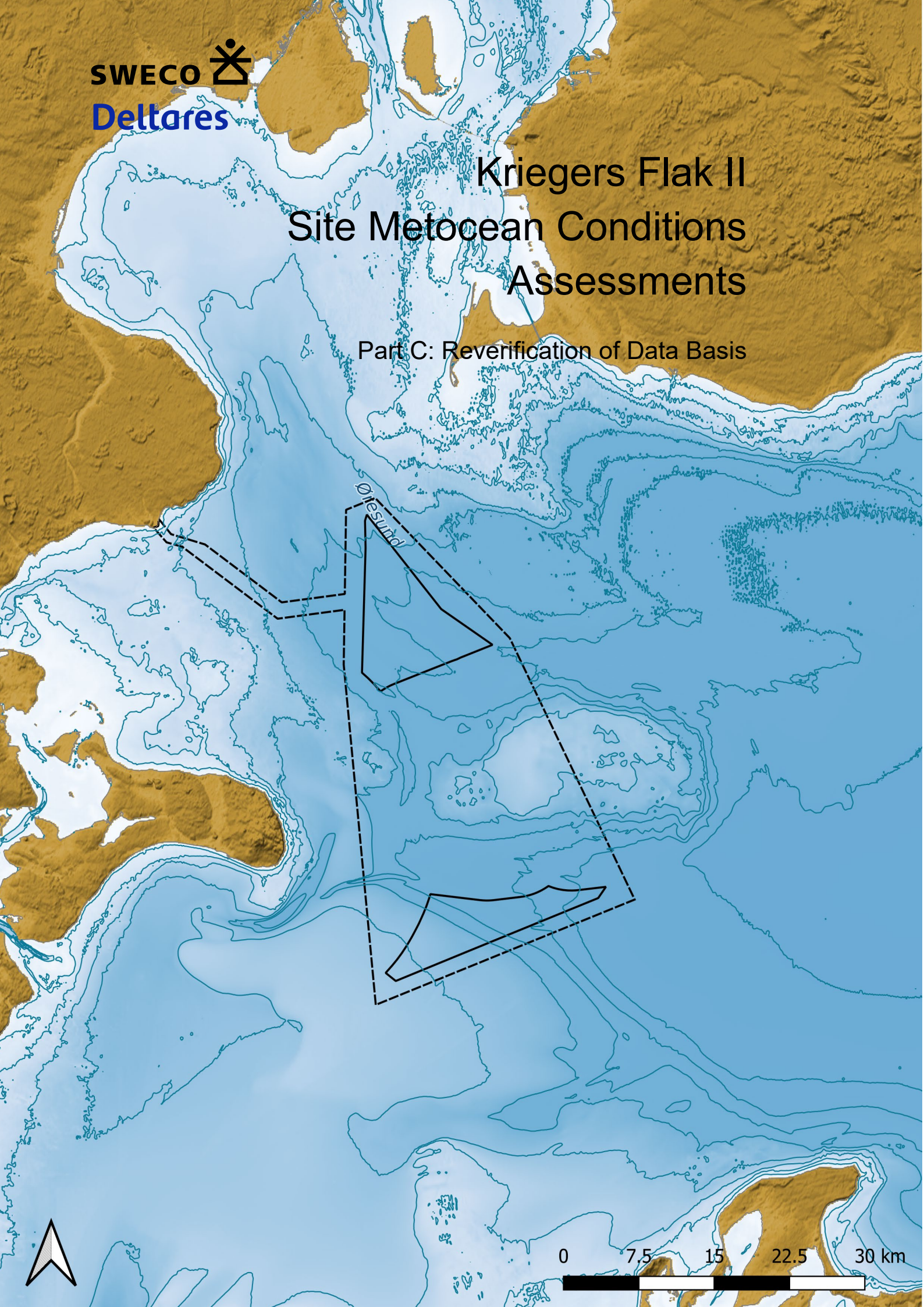





Kriegers Flak II Site Metocean Conditions Assessments

Part C: Reverification of Data Basis



Change list

Ver	Date	Description of the change	Author	Reviewed	Approved by
1	2024-11-15	New Document	Bas Reijmerink, Maria Georgiou	Sofia Caires	Jan-Joost Schouten
2	2024-12-04	Revised, final version	Bas Reijmerink, Maria Georgiou	Sofia Caires	Jan-Joost Schouten
					

Project Name	MetOcean Assessment for Kriegers Flak II North and South
Project Manager	Anders Helkjær, anders.helkjaer@sweco.dk , +4527233341
Client	Energinet Eltransmission A/S
Author	Bas Reijmerink and Maria Georgiou
Controlled by	Sofia Caires
Approved by	Jan-Joost Schouten
Date	2024-12-04
Ver	2
Document number	41011329C
Document reference	41011329C_KFII_PartC_Reverification_of_Data_Basis

Table of contents

1	Summary	11
2	Introduction	12
2.1	Background	12
2.2	Objectives	13
2.3	Approach	13
3	Overview of measurement campaign data	14
4	Wind reverification	17
4.1	Introduction	17
4.2	KFII-1 wind	17
4.3	KFII-2 wind	21
4.4	KFII-3 wind	23
5	Water level reverification	26
5.1	Introduction	26
5.2	KFII-1 water levels	26
5.3	KFII-2 water levels	29
5.4	KFII-3 water levels	32
6	Current reverification	34
6.1	Introduction	34
6.2	KFII-1 currents	34
6.3	KFII-2 currents	41
6.4	KFII-3 currents	48
7	Temperature reverification	51
8	Wave reverification	53
8.1	Introduction	53
8.2	KFII-1 waves	53
8.3	KFII-2 waves	55
8.4	KFII-3 waves	55
9	References	59
	Appendix A Error statistics	60
	Introduction	60
	Linear variables	60
	Circular variables	60
	References	62

List of Figures

Figure 2-1 Overview of the windfarm area Kriegers Flak II. The dashed line indicates the full data delivery area, and the hatched areas indicate the OWFs.	12
Figure 3-1 Instrument locations in the Kattegat and Hesselø project area. Figure taken from Fugro (2024a).	14
Figure 4-1 Timeseries comparisons between the calibrated model results and the observations from KFII-1-LB of 10 m wind speed (top panel) and direction (bottom panel). The vertical line indicates the date until which the observation data have been considered in the Deltares (2024).	18
Figure 4-2 Density scatter comparisons between the calibrated model results and the observations from KFII-1-LB of 10 m wind speed (top row) and direction (bottom row). The KFII-1-LB wind speed observations at 12 mMSL were converted to 10 mMSL. The periods covered by the data are 09-2023 to 02-2024 (left column), 02-2024 to 09-2024 (middle column) and 09-2023 to 09-2024 (right column).	19
Figure 4-3 Timeseries comparisons between the calibrated model results and the observations from KFII-1-LB of 150 m wind speed (top panel) and direction (bottom panel). The vertical line indicates the date until which the observation data have been considered in the Deltares (2024).	20
Figure 4-4 Density scatter comparisons between the calibrated model results and the observations from KFII-1-LB of 150 m wind speed (top row) and direction (bottom row). The periods covered by the data are 09-2023 to 02-2024 (left column), 02-2024 to 09-2024 (middle column) and 09-2023 to 09-2024 (right column).	20
Figure 4-5 Timeseries comparisons between the calibrated model results and the observations from KFII-2-LB of 10 m wind speed (top panel) and direction (bottom panel). The vertical line indicates the date until which the observation data have been considered in the Deltares (2024).	21
Figure 4-6 Density scatter comparisons between the calibrated model results and the observations from KFII-2-LB of 10 m wind speed (top row) and direction (bottom row). The KFII-2-LB wind speed observations at 12 mMSL were converted to 10 mMSL. The periods covered by the data are 09-2023 to 02-2024 (left column), 02-2024 to 09-2024 (middle column) and 09-2023 to 09-2024 (right column).	22
Figure 4-7 Timeseries comparisons between the calibrated model results and the observations from KFII-2-LB of 150 mMSL wind speed (top panel) and direction (bottom panel). The vertical line indicates the date until which the observation data have been considered in the Deltares (2024).	22
Figure 4-8 Density scatter comparisons between the calibrated model results and the observations from KFII-2-LB of 150 mMSL wind speed (top row) and direction (bottom row). The periods covered by the data are 09-2023 to 02-2024 (left column), 02-2024 to 09-2024 (middle column) and 09-2023 to 09-2024 (right column).	23
Figure 4-9 Timeseries comparisons between the calibrated model results and the observations from KFII-3-LB of 10 m wind speed (top panel) and direction (bottom panel). The vertical line indicates the end of 2023.	24
Figure 4-10 Density scatter comparisons between the calibrated model results and the observations from KFII-3-LB of 10 m wind speed (left) and direction (right).	24
Figure 4-11 Timeseries comparisons between the calibrated model results and the observations from KFII-3-LB of 150 mMSL wind speed (top panel) and direction (bottom panel). The vertical line indicates the end of 2023.	25
Figure 4-12 Density scatter comparisons between the calibrated model results and the observations from KFII-3-LB of 150 mMSL wind speed (left) and direction (right).	25
Figure 5-1 Timeseries comparisons between the calibrated model results and the observations from KFII-1-LB (top) and KFII-1-CP (bottom) of total water level.	27

Figure 5-2 Density scatter comparisons between the calibrated model results and the observations from KFII-1-LB water level. The plot in the top row is for the observations received during the study, the plots in the bottom row are for the final campaign observations. The periods covered by the data are 09-2023 to 02-2024 (left column), 02-2024 to 09-2024 (middle column) and 09-2023 to 09-2024 (right column).	28
Figure 5-3 Density scatter comparisons between the calibrated model results and the observations from KFII-1-CP water level. The plot in the top row is for the observations received during the study, the plots in the bottom row are for the final campaign observations. The periods covered by the data are 09-2023 to 04-2024 (left column), 04-2024 to 09-2024 (middle column) and 09-2023 to 09-2024 (right column).	29
Figure 5-4 Timeseries comparisons between the calibrated model results and the observations from KFII-2-LB (top) and KFII-2-CP (bottom) of total water level.	30
Figure 5-5 Density scatter comparisons between the calibrated model results and the observations from KFII-2-LB water level. The plot in the top row is for the observations received during the study, the plots in the bottom row are for the final campaign observations. The periods covered by the data are 09-2023 to 02-2024 (left column), 02-2024 to 09-2024 (middle column) and 09-2023 to 09-2024 (right column).	31
Figure 5-6 Density scatter comparisons between the calibrated model results and the observations from KFII-2-LB water level. The plot in the top row is for the observations received during the study, the plots in the bottom row are for the final campaign observations. The periods covered by the data are 09-2023 to 04-2024 (left column), 04-2024 to 09-2024 (middle column) and 09-2023 to 09-2024 (right column).	32
Figure 5-7 Timeseries comparisons between the calibrated model results and the observations from KFII-3-LB of total water level. The vertical red line indicates the end date of the models results in the Deltares (2024) study.	33
Figure 5-8 Density scatter comparisons between the calibrated model results and the observations from KFII-3-LB water level from 11-2023 until 04-2024.	33
Figure 6-1 Timeseries comparisons between the calibrated model results and the observations from KFII-1-LB (top) KFII-1-CP (bottom) of depth-averaged current speed.	35
Figure 6-2 Density scatter comparisons between the calibrated model results and the observations from KFII-1-LB of depth-averaged current speed. The plot in the top row is for the observations considered in Deltares (2024), the plots in the bottom row are for the final campaign observations. The periods covered by the data are 09-2023 to 02-2024 (left column), 02-2024 to 09-2024 (middle column) and 09-2023 to 09-2024 (right column).	36
Figure 6-3 Density scatter comparisons between the calibrated model results and the observations from KFII-1-CP of depth-averaged current speed. The plot in the top row is for the observations considered in Deltares (2024), the plots in the bottom row are for the final campaign observations. The periods covered by the data are 09-2023 to 04-2024 (left column), 04-2024 to 09-2024 (middle column) and 09-2023 to 09-2024 (right column).	37
Figure 6-4 Current speed Hovmöller diagrams of the calibrated model results and the observations from KFII-1-LB. The plot in the top row is with the observations considered in Deltares (2024), the plot in the bottom row is with the final campaign observations and the plot in the bottom row is with the model results.	38
Figure 6-5 Current magnitude 3D profile plots comparisons between the calibrated 3D model results (dashed lines) and the observations (full lines) from KFII-1-LB. The plot in the top row is for the observations considered in Deltares (2024), the plots in the bottom row are for the final campaign observations. The periods covered by the data are 09-2023 to 02-2024 (left column), 02-2024 to 09-2024 (middle column) and 09-2023 to 09-2024 (right column).	39
Figure 6-6 Current speed Hovmöller diagrams of the calibrated model results and the observations from KFII-1-CP. The plot in the top row is with the observations considered in Deltares (2024), the plot in the bottom row is with the final campaign observations and the plot in the bottom row is with the model results.	40

Figure 6-7 Current magnitude 3D profile plots comparisons between the calibrated 3D model results (dashed lines) and the observations (full lines) from KFII-1-CP. The plot in the top row is for the observations considered in Deltares (2024), the plots in the bottom row are for the final campaign observations. The periods covered by the data are 09-2023 to 04-2024 (left column), 04-2024 to 09-2024 (middle column) and 09-2023 to 09-2024 (right column).....	41
Figure 6-8 Timeseries comparisons between the calibrated model results and the observations from KFII-2-LB of depth-averaged current speed.....	42
Figure 6-9 Density scatter comparisons between the calibrated model results and the observations from KFII-2-LB of depth-averaged current speed. The plot in the top row is for the observations considered in Deltares (2024), the plots in the bottom row are for the final campaign observations. The final campaign data contains no valid data outside the period considered in Deltares (2024).	43
Figure 6-10 Density scatter comparisons between the calibrated model results and the observations from KFII-2-CP of depth-averaged current speed. The plot in the top row is for the observations considered in Deltares (2024), the plots in the bottom row are for the final campaign observations. The periods covered by the data are 09-2023 to 04-2024 (left column), 04-2024 to 09-2024 (middle column) and 09-2023 to 09-2024 (right column).....	44
Figure 6-11 Current speed Hovmöller diagrams of the calibrated model results and the observations from KFII-2-LB. The plot in the top row is with the observations considered in Deltares (2024), the plot in the bottom row is with the final campaign observations and the plot in the bottom row is with the model results.....	45
Figure 6-12 Current magnitude 3D profile plots comparisons between the calibrated 3D model results (dashed lines) and the observations (full lines) from KFII-2-LB. The plot in the top row is for the observations considered in Deltares (2024), the plots in the bottom row are for the final campaign observations. The final campaign data contains no valid data outside the period considered in Deltares (2024).	46
Figure 6-13 Current speed Hovmöller diagrams of the calibrated model results and the observations from KFII-2-CP. The plot in the top row is with the observations considered in Deltares (2024), the plot in the bottom row is with the final campaign observations and the plot in the bottom row is with the model results.....	47
Figure 6-14 Current magnitude 3D profile plots comparisons between the calibrated 3D model results (dashed lines) and the observations (full lines) from KFII-2-CP. The plot in the top row is for the observations considered in Deltares (2024), the plots in the bottom row are for the final campaign observations. The periods covered by the data are 09-2023 to 04-2024 (left column), 04-2024 to 09-2024 (middle column) and 09-2023 to 09-2024 (right column).....	48
Figure 6-15 Timeseries comparisons between the calibrated model results and the observations from KFII-3-LB of depth-averaged current speed. The vertical red line indicates the end date of the models results in the Deltares (2024) study.	49
Figure 6-16 Density scatter comparisons between the calibrated model results and the observations from KFII-3-LB of depth-averaged current from 11-2023 to 04-2024.	49
Figure 6-17 Current speed Hovmöller diagrams of the observations (top panel) and the calibrated model results (bottom panel) from KFII-3-CP.	50
Figure 6-18 Current magnitude 3D profile plots comparisons between the calibrated 3D model results (dashed lines) and the observations (full lines) from KFII-3-LB from 11-2023 to 04-2024.	50
Figure 7-1 Hovmöller diagrams of the 3D temperature model results (background colour map) and near-bottom and near-surface temperature observations (coloured circles) from KFII-1-CP and KFII-1-LB, respectively. The vertical line indicates the date until which the observation data have been considered in the Deltares (2024).	51
Figure 7-2 Hovmöller diagrams of the 3D temperature model results (background colour map) and near-bottom and near-surface temperature observations (coloured circles) from KFII-2-CP and KFII-2-LB, respectively. The vertical line indicates the date until which the observation data have been considered in the Deltares (2024).	51

Figure 7-3 Hovmöller diagrams of the 3D temperature model results (background colour map) and near-surface temperature observations (coloured circles) from KFII-3-LB. The vertical line indicates the date until which the observation data have been considered in the Deltares (2024).	52
Figure 8-1 Timeseries comparisons between the calibrated model results and the observations from KFII-1-LB of significant wave height (top panel), peak wave period (middle panel) and mean wave direction (bottom panel). The vertical line indicates the date until which the observation data have been considered in the Deltares (2024).	54
Figure 8-2 Density scatter comparisons between the calibrated model results and the observations from KFII-1-LB of significant wave height (top row), peak wave period (middle row) and mean wave direction (bottom row). The periods covered by the data are 09-2023 to 12-2023 (left column), 01-2024 to 09-2024 (middle column) and 09-2023 to 09-2024 (right column).	55
Figure 8-3 Timeseries comparisons between the calibrated model results and the observations from KFII-2-LB of significant wave height (top panel), peak wave period (middle panel) and mean wave direction (bottom panel). The vertical line indicates the date until which the observation data have been considered in the Deltares (2024).	56
Figure 8-4 Density scatter comparisons between the calibrated model results and the observations from KFII-2-LB of significant wave height (top row), peak wave period (middle row) and mean wave direction (bottom row). The periods covered by the data are 09-2023 to 12-2023 (left column), 01-2024 to 09-2024 (middle column) and 09-2023 to 09-2024 (right column).	57
Figure 8-5 Timeseries comparisons between the calibrated model results and the observations from KFII-3-LB of significant wave height (top panel), peak wave period (middle panel) and mean wave direction (bottom panel). The vertical line indicates the end of 2023.	58
Figure 8-6 Density scatter comparisons between the calibrated model results and the observations from KFII-3-LB of significant wave height (left), peak wave period (middle) and mean wave direction (right).	58

List of Tables

Table 3-1 Coordinates of the KFII-1, KFII-2 and KFII-3 stations.	14
Table 3-2 Considered KFII-1, KFII-2 and KFII-3 observation data.....	16

Nomenclature

Variable	Abbreviation	Unit
Atmosphere		
Wind speed @ 10 mMSL height	U _{10mag}	m/s
Wind direction @ 10 mMSL height	U _{10dir}	°N (clockwise from)
Wind speed @ 150 m MSL height	U _{150mag}	m/s
Wind direction @ 150 mMSL height	U _{150dir}	°N (clockwise from)
Ocean		
Water level	WL or SWL	mMSL
Current speed	CS or u or u _{yy,xx} (yy=total, tide, res, xx=level or DA)	m/s
Current direction	CD or u _{dir} or u _{dir,yy,xx} (yy=total, tide, res, xx=level or DA)	°N (clockwise to)
Sea surface temperature	SST	°C
Water temperature @ {x} m depth	Tsw{x}	°C
Waves		
Significant wave height	H _{m0} or H _s	m
Peak wave period	T _p	s
Mean wave direction	MWD	°N (clockwise from)
Definitions		
Coordinate System	WGS84 EPSG 4326 (unless specified differently)	
Direction	Clockwise from North	
Wind	°N coming from	
Current	°N going to	
Waves	°N coming from	
Time	Times are relative to UTC	
Vertical Datum	MSL (unless specified differently)	
Statistics		
RMSE	root-mean-square error	
ρ	correlation coefficient	
σ	standard deviation	
R	symmetric slope	
n	sample size	
Abbreviations		

3D	3-dimensional
DMI	Danish Meteorological Institute
DNV	Det Norske Veritas
ECMWF	European Centre for Medium-Range Weather Forecasts
EMODnet	The European Marine Observation and Data Network
ERA5	ECMWF Re-analysis v5
FEED	Front-End Engineering Design
IEC	International Electrotechnical Commission
ISO	International Organization for Standardization
KFII	Kriegers Flak II North and South
mMSL	Metres above Mean Sea Level
MSL	Mean Sea Level
OWF	Offshore Wind Farm
UTC	Coordinated Universal Time
WGS84	World Geodetic System 1984

1 Summary

The Danish Energy Agency has tasked Energinet (the Client) with undertaking site metocean conditions assessments for the development of the offshore wind farm areas Kriegers Flak II North and South. So far, the study involved the metocean data basis report and the database (Part A) and the metocean data analysis report (parts B).

This note presents the reverification of the metocean hindcast data used as input in the assessments of the metocean site conditions. More precisely, in this reverification note, measurements from the metocean measurement campaigns carried out in the offshore wind farm areas Kriegers Flak II North and South and, which were still not available at the time the metocean study was carried out, are compared to metocean hindcast data produced and calibrated in the same way as the data in the metocean database (Part A report, Deltares, 2024). The parameters considered in this reverification note are wind speed and direction, wave height, period and direction, current speed, still water level and water temperature. The conclusion is that the reverification of all the parameters mentioned does not change any of the conclusions made in the Part A report. The quality of the basis data is as reported and there is no need for recalibration.

2 Introduction

2.1 Background

The Danish Energy Agency has tasked Energinet (ENDK, the Client) with undertaking site metocean conditions assessments for the development of the offshore wind farm areas Kriegers Flak II North and South. The offshore wind farms are to be in the Southwestern part of the Baltic Sea east of Sjælland. An overview is shown in Figure 2-1.

The site metocean conditions assessments, which are to be certified, will form part of the larger site conditions assessment work (also including site wind and ice conditions assessments) and will be a part of the technical basis for the future public tender on the development of offshore wind farms within the areas. The site metocean conditions assessment must be suitable for the Front-End Engineering and Design (FEED) of offshore WTG and other support structures for the offshore wind farms.



Figure 2-1 Overview of the windfarm area Kriegers Flak II. The dashed line indicates the full data delivery area, and the hatched areas indicate the OWFs.

The full study consists of several deliverables:

- Part A: Description and Verification of Data Basis (Deltares, 2024).
- Part B: Data Analyses and Results (Sweco, 2024).
- Long-term hindcast data (digital timeseries, delivered with Part A, Deltares, 2024).

- Measurement data (digital timeseries, Fugro, 2024a,b).
- Part C: Reverification of Data Basis (this report).

All deliverables except for Part C, this report, are already completed.

2.2 Objectives

In Part A of the study metocean data, which serves as input for the assessment of the MetOcean site conditions to support the design of the various structures within the offshore wind farm areas Kriegers Flak II North and South have been derived. These data, which originate from hourly model results covering a long period, namely from 1979 until 2023, have been validated and calibrated using measurement data available in the area. In particular data from the metocean measurement campaign carried out by Fugro have been used to validate and calibrate the model results. However, at the time of the Part A study the full metocean measurement campaign data were not yet available. The campaigns took place from 03-09-2023 to 03-09-2024 and in the Part A study data until up to April 2024 have been considered.

The measurement campaigns are now ended and Fugro (2024a,b) has quality controlled the whole campaigned data and released the final metocean campaign datasets. The purpose of this note is to reverify metocean hindcast data produced and calibrated in the same way as the data in the metocean database (Part A report, Deltares, 2024) using measurements from the metocean measurement campaigns carried out in the offshore wind farm areas Kriegers Flak II North and South and which were not considered in Deltares (2024).

2.3 Approach

The computations of Deltares (2024) have been extended until the end of September 2024 using the same models and applying the same calibration factors as in the derivation of deliverable “Long-term hindcast data” (digital timeseries, delivered with Part A report, Deltares, 2024). These data are compared with the full campaign data for the period considered in Deltares (2024), the period for which data are now available and which had not been considered in Deltares (2024) and the full campaign data. The aim of the comparisons is to identify whether the quality of the model results considering the extra measurement data is comparable to the quality assessed in the data basis study (Deltares, 2024). The variables being considered are wind speed, water level, current speed, significant wave height, peak wave period and mean wave direction. The comparisons are made qualitatively by means of timeseries and Hovmöller plots and quantitatively by means of density scatter plots, quantile-quantile comparisons and errors statistics. In addition, for currents, the vertical current speed profiles are also compared.

Because the water level and current data can contain inhomogeneities due to variations in the location of the sensors, deterioration of the current speed signal due to interferences or contaminations, the final quality assured dataset can differ significantly from the monthly datasets delivered during the campaign. Because of this, in the comparisons between the water level and current model results with the observations we also plot the observation data considered in Deltares (2024). The difference between the monthly and the final wave and wind data are generally not significant and, therefore, in the reverification of the wind and wave data we only consider the final campaign data.

3 Overview of measurement campaign data

The Kriegers Flak II metocean measurement campaign described in Fugro (2024a,b) was carried out at three location KFII-1, KFII-2 and KFII-3. KFII-1 is located in Kriegers Flak II south and KFII-2 and KFII-3 in Kriegers Flak II north. The locations where the instruments have been deployed are shown in Figure 3-1 and the coordinates are given in Table 3-1.

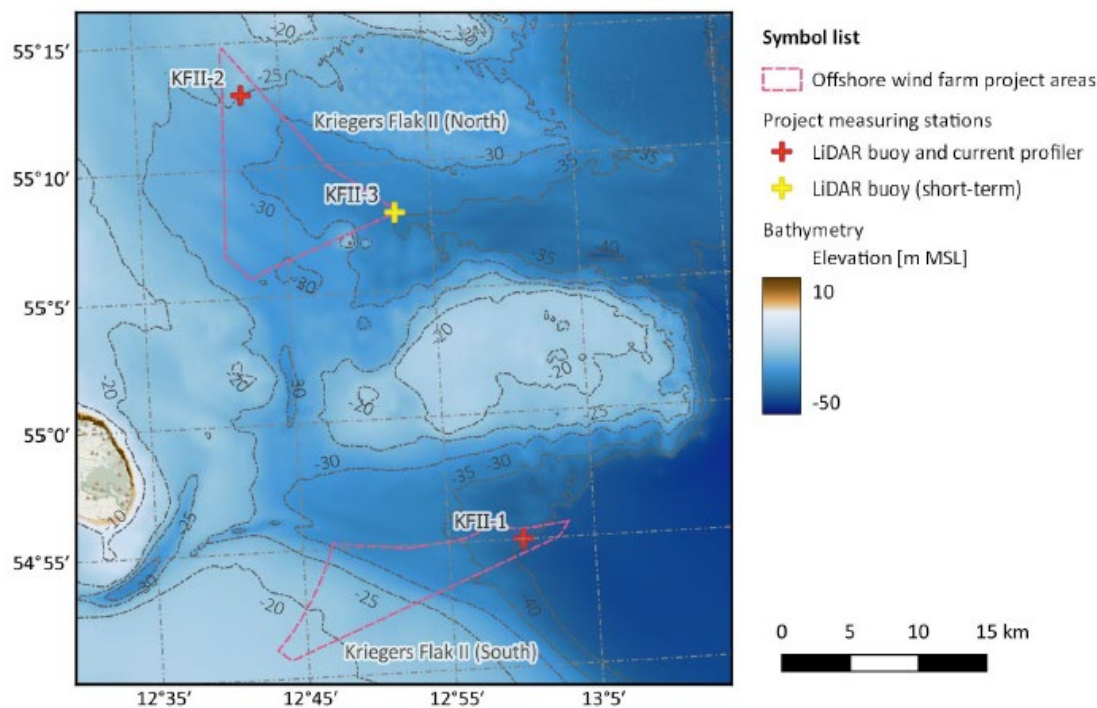


Figure 3-1 Instrument locations in the Kattegat and Hesselø project area. Figure taken from Fugro (2024a).

Table 3-1 Coordinates of the KFII-1, KFII-2 and KFII-3 stations.

Station	Longitude (°E)	Latitude (°N)	Depth (mMSL)
KFII-1-LP	12.9945	54.9168	39.7
KFII-1-CP	12.9939	54.9167	39.6
KFII-2-LP	12.6986	55.2156	27.2
KFII-2-CP	12.6992	55.2153	27.3
KFII-3-LB	12.8681	55.1348	32.9

The KFII-1 campaign (Fugro, 2024a) included a LiDAR buoy with a bottom mounted water level sensor, station KFII-1-LB, and a bottom mounted upward-looking current profiler, station KFII-1-CP. During the campaign two LiDAR buoys have been deployed:

- Lidar buoy WS190 from 03-09-2023 to 16-02-2024 and
- Lidar buoy WS172 from 16-02-2024 to 03-09-2024.

The instruments in the buoy include the wind LiDAR, the wave sensor and the downward - looking current profiler. During the campaign period two upward-looking current profilers have been deployed:

- 104620 from 03-09-2023 to 15-04-2024 (D1) and
- 104503 from 15-04-2023 to 03-09-2024 (D2).

The KFII-2 campaign (Fugro, 2024a) included a LiDAR buoy with a bottom mounted water level sensor, station KFII-2-LB, and a bottom mounted upward-looking current profiler, station KFII-2-CP. During the campaign three LiDAR buoys have been deployed:

- Lidar buoy WS172 from 03-09-2023 to 16-01-2024
- Lidar buoy SWLB085 from 16-01-2024 to 07-06-2024 and
- Lidar buoy SWLB083 from 07-06-2024 to 03-09-2024.

The instruments in the buoy include the wind LiDAR, the wave sensor and the downward - looking current profiler. During the campaign period two upward-looking current profilers have been deployed:

- 104621 from 03-09-2023 to 15-04-2024 (D1) and
- 104620 from 15-04-2023 to 03-09-2024 (D2).

At KFII-3 only LiDAR buoy (WS210) with a bottom mounted water level sensor has been deployed 01-11-2023 to 14-04-2024 from (Fugro, 2024b), station KFII-3-LB. The KFII-3-LB current data are available with 1 m intervals from -3 to -31 mMSL. These data have not been considered in Deltares (2024).

Table 3-2 provides an overview of the instruments and considered variables.

Table 3-2 Considered KFII-1, KFII-2 and KFII-3 observation data.

Station	Sensor	Variable	Period
KFII-1-LB, KFII-2-LB and KFII-3-LB	Wind: ZephIR ZX300M CW LiDAR	12 mMSL and 150 mMSL wind speed and direction	09-2023 – 09-2024
KFII-1-LB, KFII-2-LB and KFII-3-LB	WL (bottom pressure): Thelma Biotel TBR700	Water pressure and water level	09-2023 – 09-2024
KFII-1-LB	Current: Nortek Aquadopp 400 kHz	Current speed at 1 m intervals from -3 to -33 mMSL	09-2023 – 09-2024
KFII-2-LB	Current: Nortek Aquadopp 400 kHz	Current speed at 1 m intervals from -3 to -26 mMSL	09-2023 – 09-2024
KFII-3-LB	Current: Nortek Aquadopp 400 kHz	Current speed at 1 m intervals from -3 to -31 mMSL	11-2023 – 04-2024
KFII-1-LB, KFII-2-LB and KFII-3-LB	Waves: Wavesense 3	H _s , T _p , MWD	09-2023 – 09-2024
KFII-1-CP	WL (Bottom pressure) and Current: Nortek Signature 500	Water pressure, water level and current speed at 1 m intervals at 5 to 34 m from bottom	09-2023 – 04-2024 (D1) and 04-2024 – 09-2024 (D2)
KFII-2-CP	WL (Bottom pressure) and Current: Nortek Signature 500	Water pressure, water level and current speed at 1 m intervals at 4 to 24 m from bottom	09-2023 – 04-2024 (D1) and 04-2024 – 09-2024 (D2)

4 Wind reverification

4.1 Introduction

The following sections 4.2, 4.3 and 4.4 show the comparisons between the calibrated model results and the observations of wind from KFII-1, KFII-2 and KFII-3, respectively. The considered variables are the 10 m and the 150 m (hub height) wind speeds and directions.

4.2 KFII-1 wind

Figure 4-1 shows the timeseries comparisons between the model data of wind speed and direction at 10 mMSL and the LiDAR observations of wind speed and direction at 12 mMSL converted to 10 mMSL at KFII-1-LB. In this and other timeseries figures in this report, the red vertical line indicates the period until which the observation data have been considered in the validation of the model results for the variable in question in Deltares (2024).

Figure 4-2 shows the density scatter comparisons between the calibrated model results and the observations of wind speed and direction at 10 m for three periods:

1. the period considered in Deltares (2024), i.e. the period until the red line in Figure 4-1,
2. the extra campaign data period, of which the observations were not considered in Deltares (2024), i.e. the period after the red line in Figure 4-1, and
3. the whole campaign period.

In the density scatter comparison plots in Figure 4-2 and other in this report, the colours indicate the data density, with darker colours indicating higher data density. The plots include main statistics of the data comparisons such as the correlation coefficient, root-mean-square errors, bias and standard deviation between the datasets. Appendix A describes of how these statistics were computed. The presented statistics depend on whether linear (speeds, heights and periods), as in the top panels of Figure 4-2, or circular (directions) variables, as in the bottom panels of Figure 4-2 are plotted. Furthermore, in the plots of linear variables, the plots also include percentile comparisons and two fits are given: a symmetric fit (red dotted line) to the whole data (plotted in terms of density) and a linear fit (dashed blue line) through the data percentiles (the blue pluses, with each one corresponding to one percentile pair, 101 pluses in total, indicating the 1.00th to the 99.00th with increases of 1 and the 99.90th and the 99.99th). The red line provides an indication of the relation between the bulk of the data. The symmetric slop is given as it provides a direct measure of the (percentage of) over- or underestimation. The blue line provides an indication of the linear relation between the data extremes, with the considered percentiles being the plotted 1st to the 99.99th.

Figure 4-1 shows that the wind speeds in the period of the KFII-1-LB campaign which is not considered in Deltares (2024), February to September 2024, is milder than the period before, September 2023 to February 2024. Nevertheless, Figure 4-1 and Figure 4-2 show that the correspondence between the model results and the KFII-1-LB observations is similar in the considered periods with comparable coefficients, in spite of the correlations being as expected slightly lower in the milder period.

Figure 4-3 shows the timeseries comparisons between the model results and the observations of the 150 m wind speeds and directions at KFII-1-LB. The respective density scatter comparisons are given in Figure 4-4. The figures show also that the correspondence between the model results and the KFII-1-LB observations of the 150 m wind speeds and directions is also similar in the considered periods, with comparable correlation and fit coefficients, in spite of slightly lower correlations in the milder period.

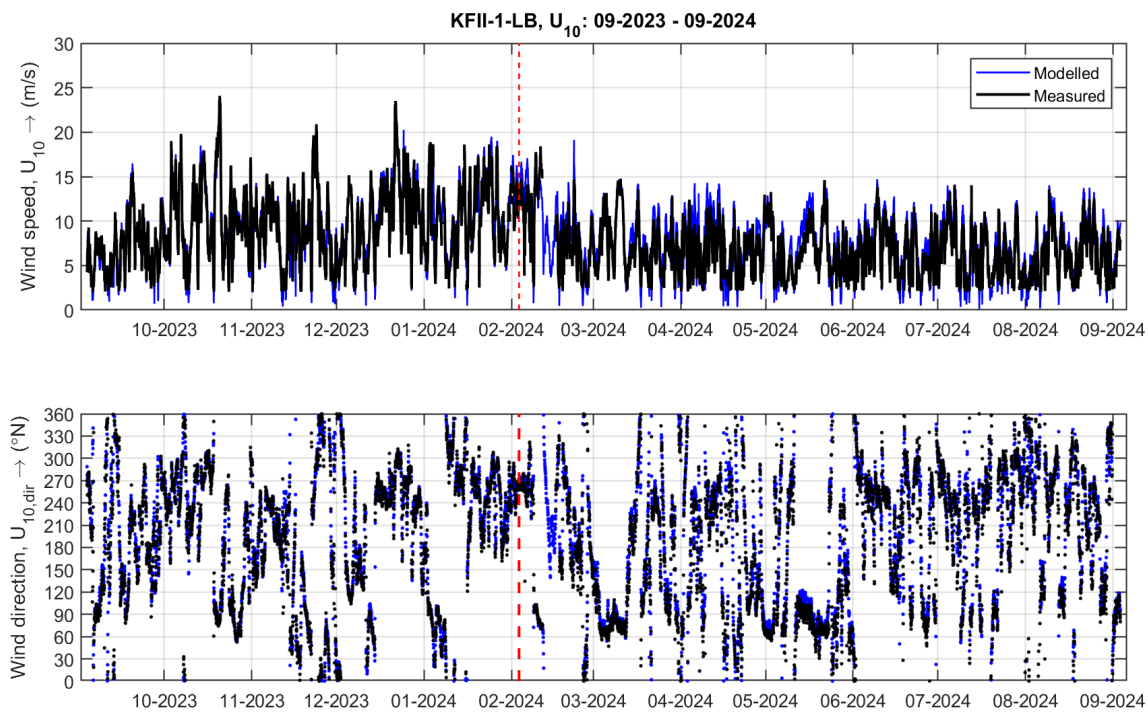


Figure 4-1 Timeseries comparisons between the calibrated model results and the observations from KFII-1-LB of 10 m wind speed (top panel) and direction (bottom panel). The vertical line indicates the date until which the observation data have been considered in the Deltares (2024).

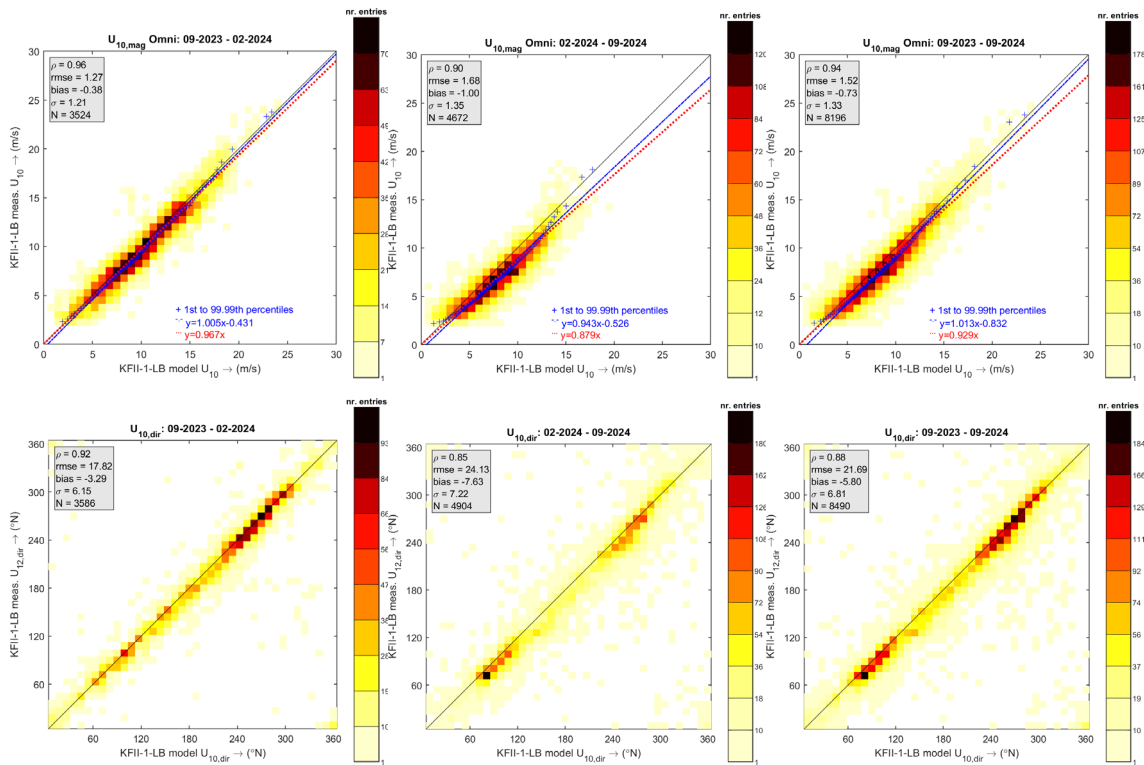


Figure 4-2 Density scatter comparisons between the calibrated model results and the observations from KFII-1-LB of 10 m wind speed (top row) and direction (bottom row). The KFII-1-LB wind speed observations at 12 mMSL were converted to 10 mMSL. The periods covered by the data are 09-2023 to 02-2024 (left column), 02-2024 to 09-2024 (middle column) and 09-2023 to 09-2024 (right column).

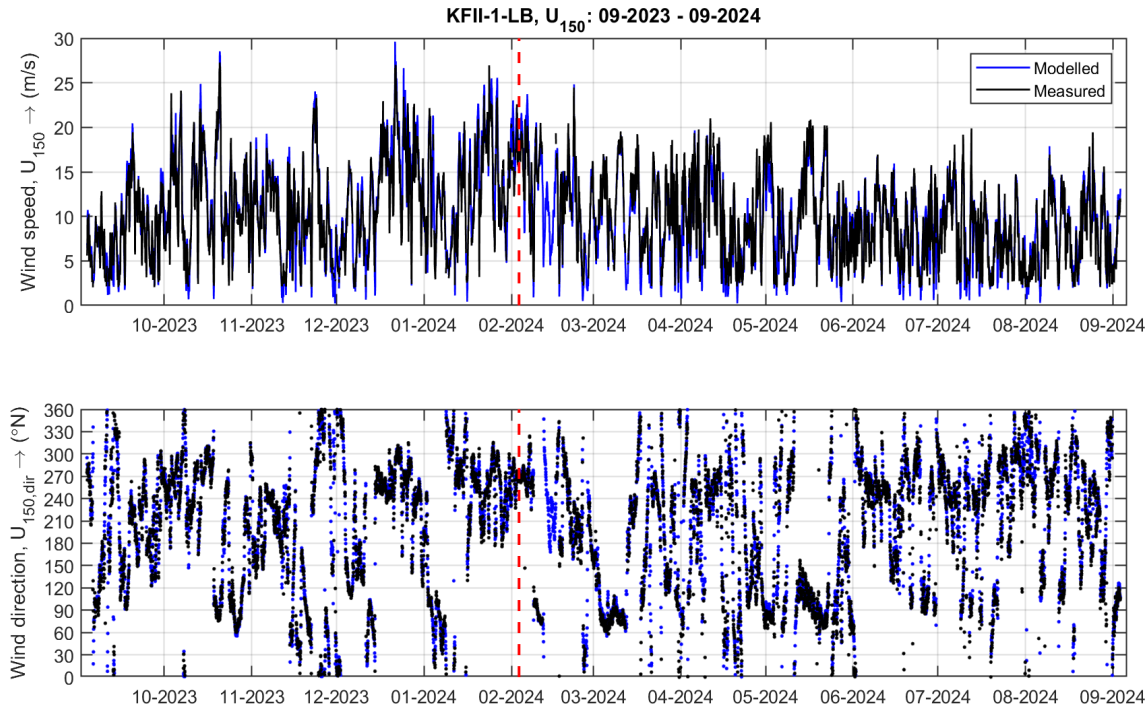


Figure 4-3 Timeseries comparisons between the calibrated model results and the observations from KFII-1-LB of 150 m wind speed (top panel) and direction (bottom panel). The vertical line indicates the date until which the observation data have been considered in the Deltares (2024).

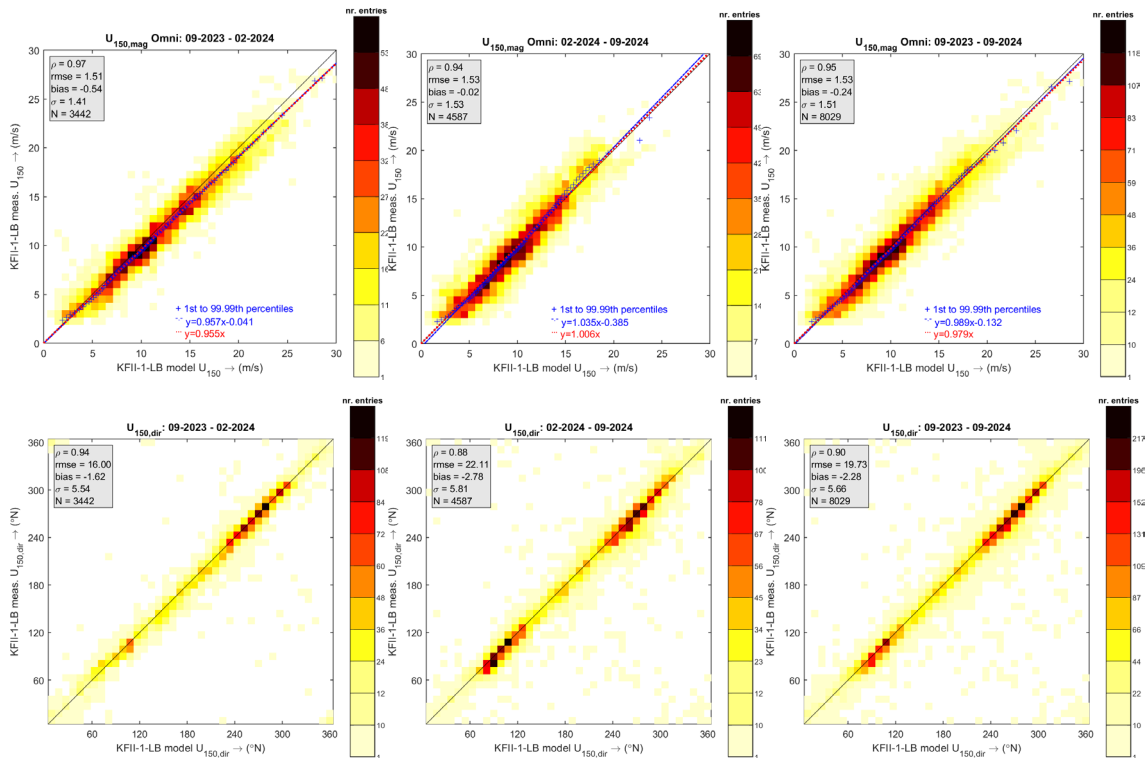


Figure 4-4 Density scatter comparisons between the calibrated model results and the observations from KFII-1-LB of 150 m wind speed (top row) and direction (bottom row). The periods covered by the data are 09-2023 to 02-2024 (left column), 02-2024 to 09-2024 (middle column) and 09-2023 to 09-2024 (right column).

4.3 KFII-2 wind

Figure 4-5 shows the timeseries comparisons between the model data of wind speed and direction at 10 m and the observations at 12 mMSL of wind speed and direction converted to 10 mMSL at KFII-2-LB. Figure 4-6 shows the respective density scatter comparisons in the considered three periods. Figure 4-7 shows the timeseries comparisons between the model results and the observations of the 150 m wind speeds and directions at KFII-2-LB. The respective density scatter comparisons are given in Figure 4-8.

The timeseries figures show again that the data from the period not considered in Deltares (2024) are milder, leading to as expected a slightly lower correlation between the modelled and observed wind speeds, but the correspondence between the model results and the observations for the different time periods is still high and comparable. The density scatter plots also show that the error statistics are also very similar in the considered three periods of data.

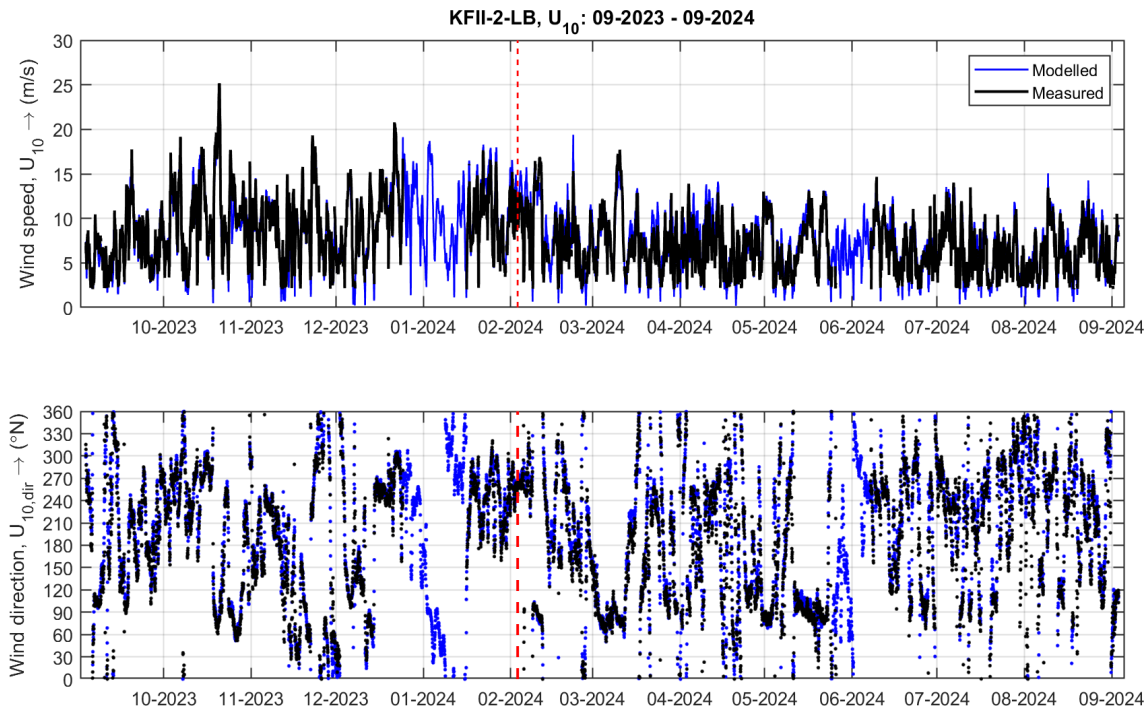


Figure 4-5 Timeseries comparisons between the calibrated model results and the observations from KFII-2-LB of 10 m wind speed (top panel) and direction (bottom panel). The vertical line indicates the date until which the observation data have been considered in the Deltares (2024).

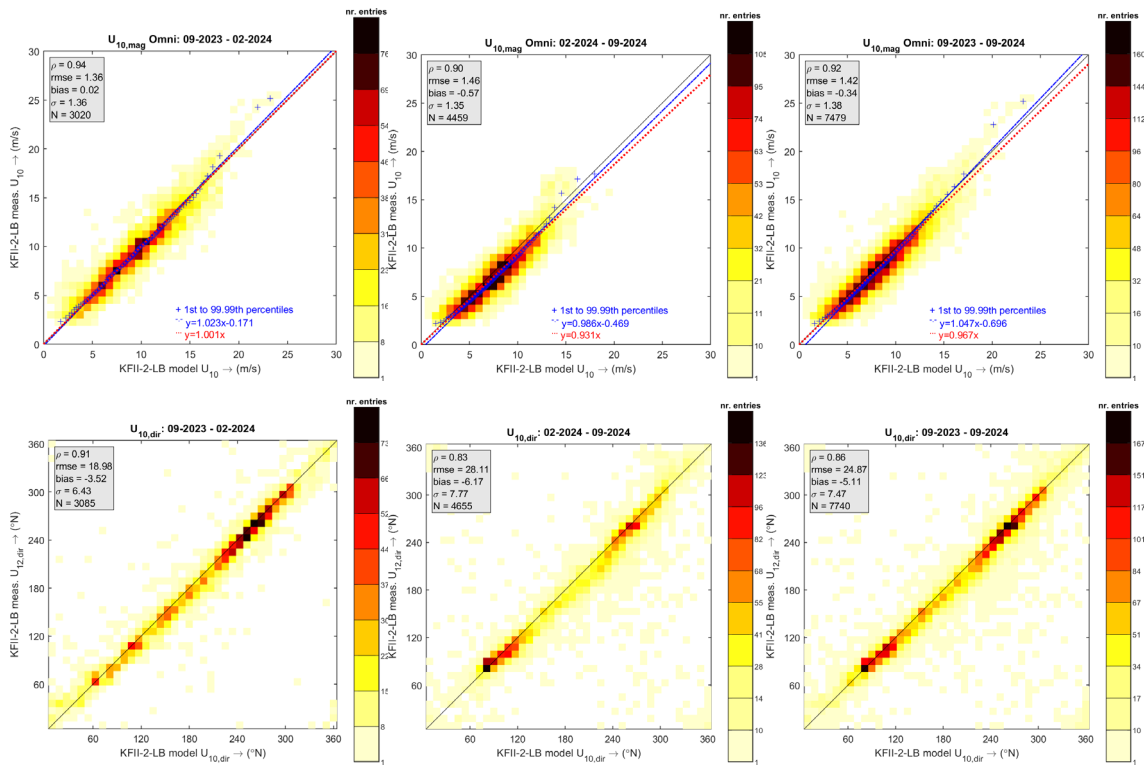


Figure 4-6 Density scatter comparisons between the calibrated model results and the observations from KFII-2-LB of 10 m wind speed (top row) and direction (bottom row). The KFII-2-LB wind speed observations at 12 mMSL were converted to 10 mMSL. The periods covered by the data are 09-2023 to 02-2024 (left column), 02-2024 to 09-2024 (middle column) and 09-2023 to 09-2024 (right column).

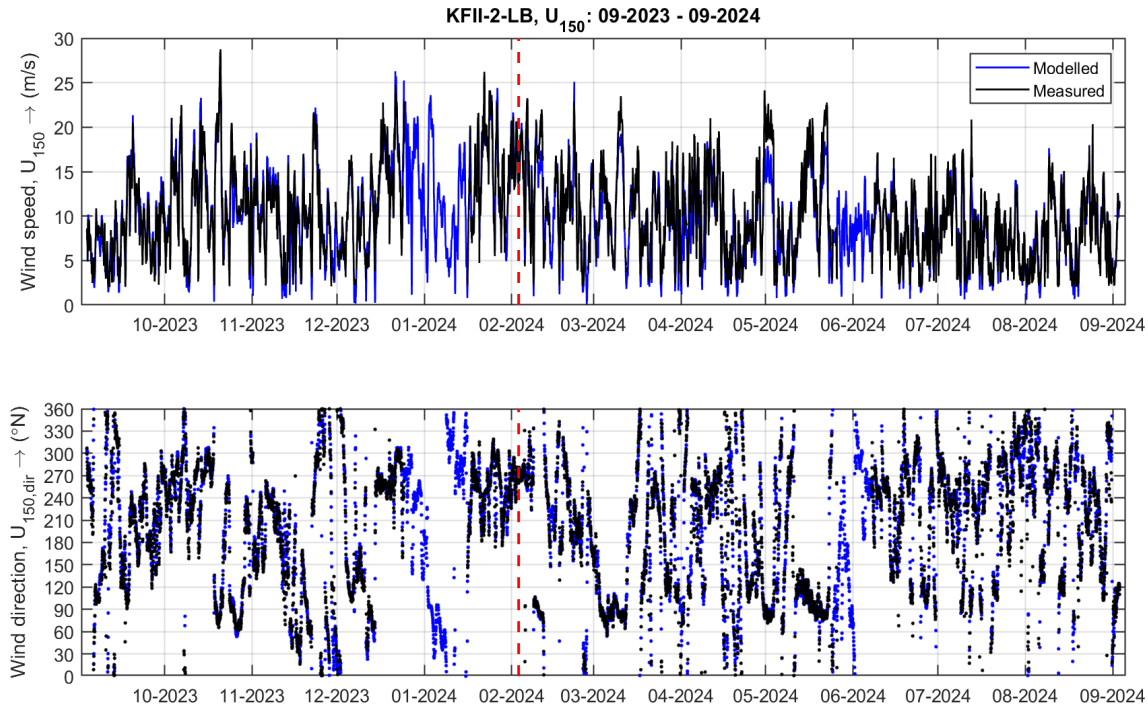


Figure 4-7 Timeseries comparisons between the calibrated model results and the observations from KFII-2-LB of 150 mMSL wind speed (top panel) and direction (bottom panel). The vertical line indicates the date until which the observation data have been considered in the Deltares (2024).

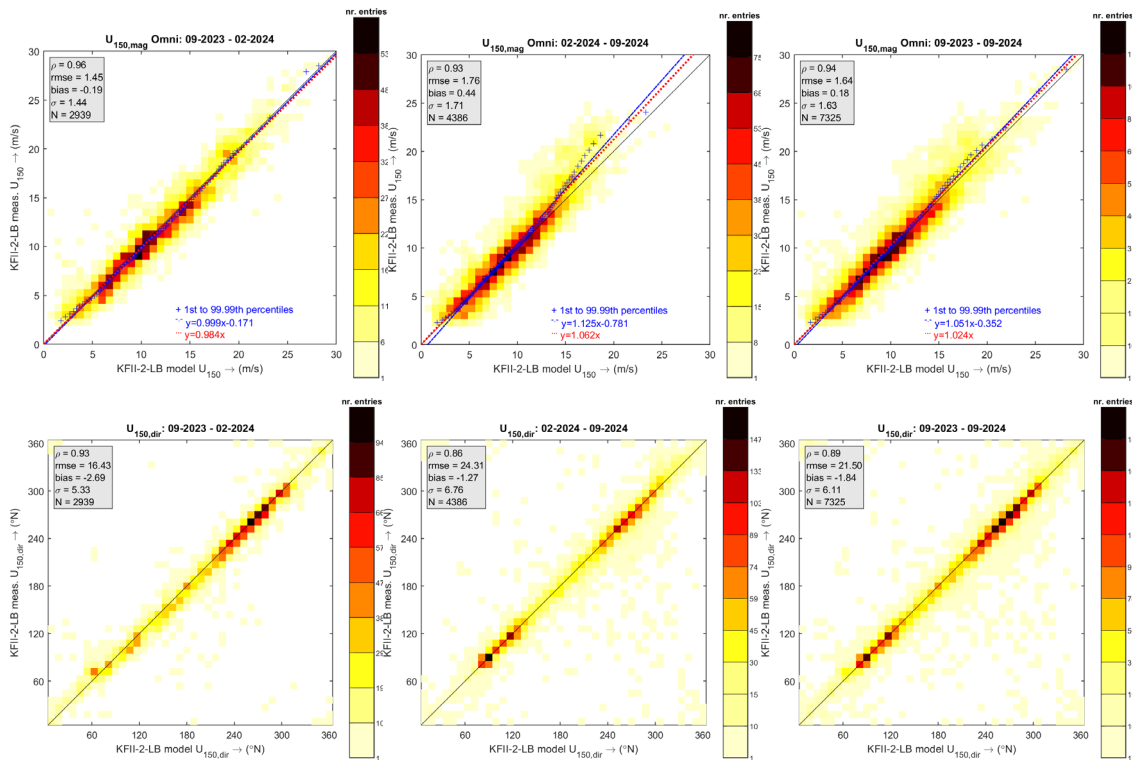


Figure 4-8 Density scatter comparisons between the calibrated model results and the observations from KFI-2-LB of 150 mMSL wind speed (top row) and direction (bottom row). The periods covered by the data are 09-2023 to 02-2024 (left column), 02-2024 to 09-2024 (middle column) and 09-2023 to 09-2024 (right column).

4.4 KFII-3 wind

Figure 4-9 shows the timeseries comparisons between the model data of wind speed and direction at 10 mMSL and the observations 12 mMSL observations of wind speed and direction converted to 10 mMSL at KFII-3-LB. Figure 4-10 shows the respective density scatter comparisons in the considered three periods. Figure 4-11 shows the timeseries comparisons between the model results and the observations of the 150 mMSL wind speeds and directions at KFII-3-LB. The respective density scatter comparisons are given in Figure 4-12. The KFII-3 data have not been considered in Deltares (2024) as it were not yet available then. The density scatter comparisons are therefore for the full campaign period. The figures show that as for the observations from KFII-1-LB and KFII-2-LB, the agreement between the model results and the observations is high, with correlations of 0.93-0.96 for wind speed and of 0.91-0.92 for wind direction. The figures also show that the model results slightly overestimate the surface wind speeds. This extra comparisons confirm the validity of the model results.

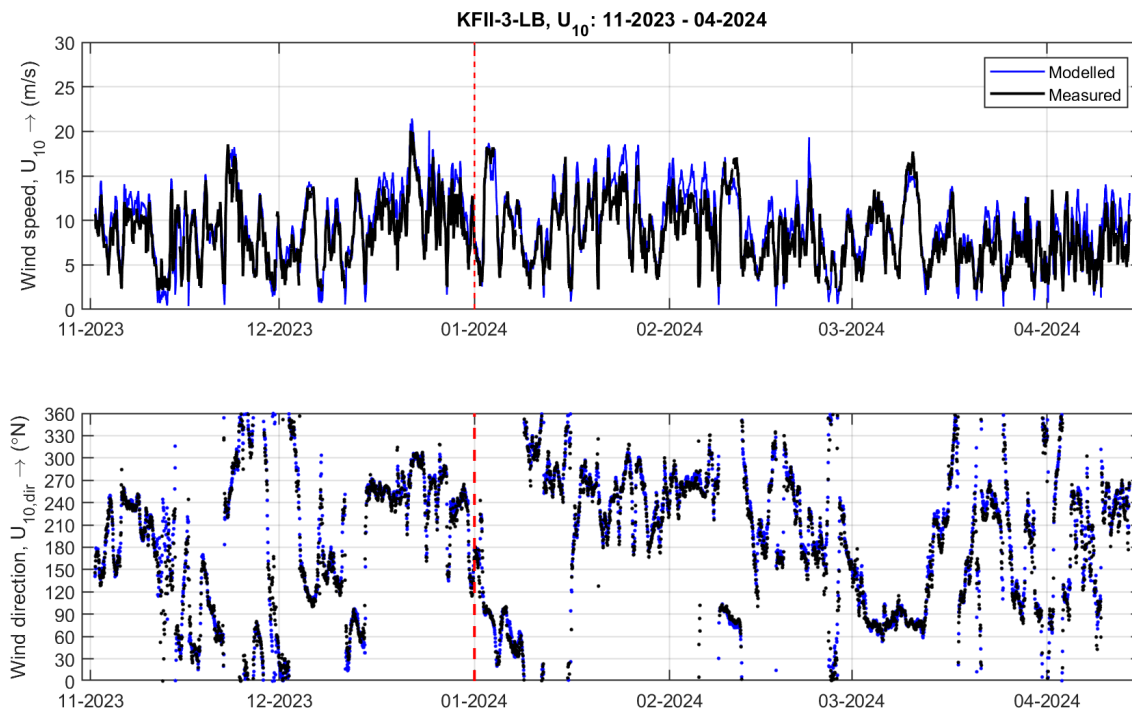


Figure 4-9 Timeseries comparisons between the calibrated model results and the observations from KFII-3-LB of 10 m wind speed (top panel) and direction (bottom panel). The vertical line indicates the end of 2023.

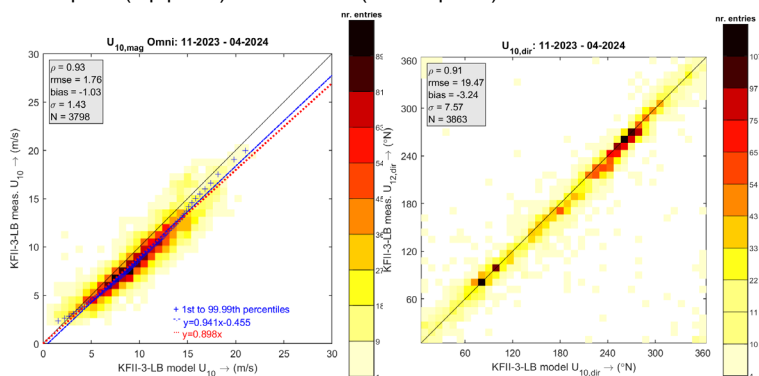


Figure 4-10 Density scatter comparisons between the calibrated model results and the observations from KFII-3-LB of 10 m wind speed (left) and direction (right).

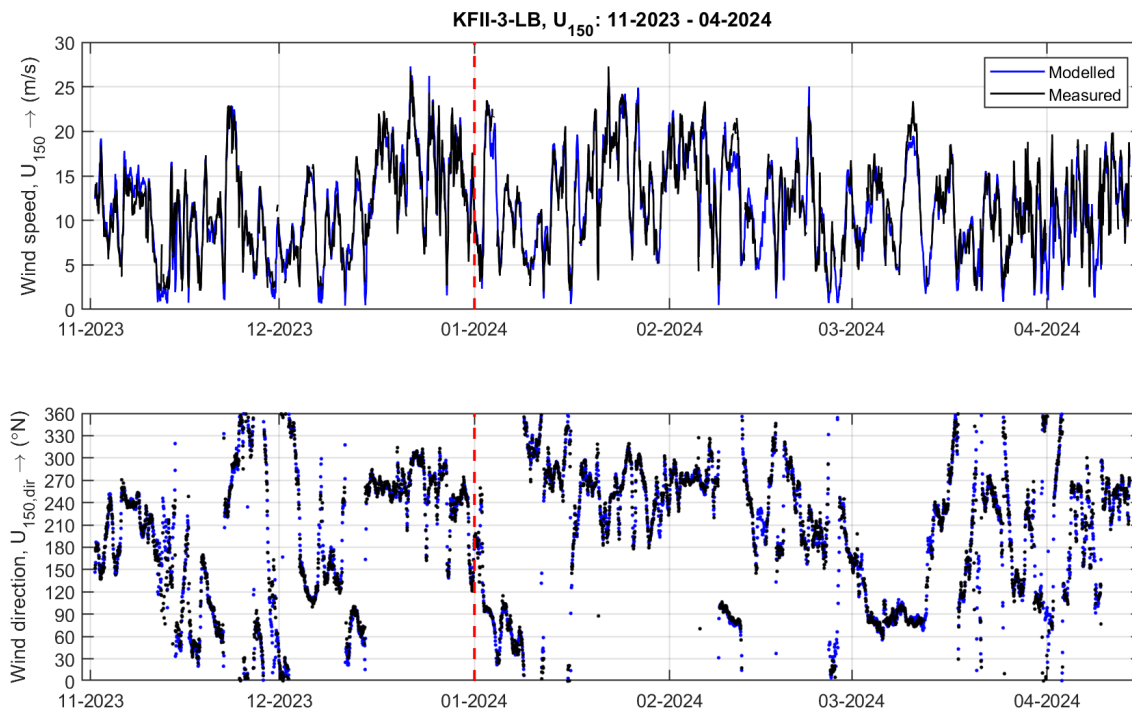


Figure 4-11 Timeseries comparisons between the calibrated model results and the observations from KFII-3-LB of 150 mMSL wind speed (top panel) and direction (bottom panel). The vertical line indicates the end of 2023.

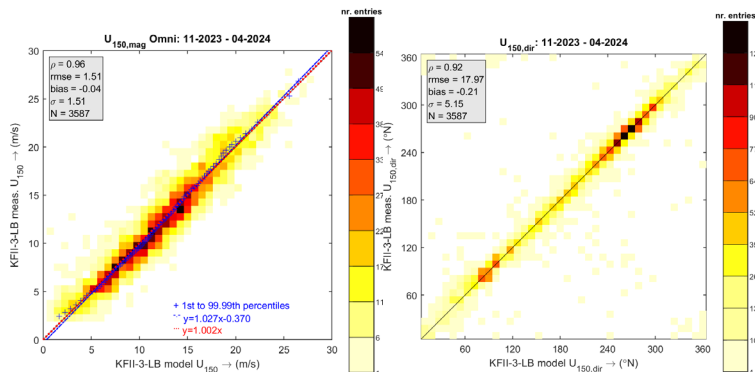


Figure 4-12 Density scatter comparisons between the calibrated model results and the observations from KFII-3-LB of 150 mMSL wind speed (left) and direction (right).

5 Water level reverification

5.1 Introduction

The following sections 5.2, 5.3 and 5.4 show the comparisons between the calibrated model results and the water level observations from KFII-1, KFII-2 and KFII-3, respectively.

The bottom-mounted instruments used in the Fugro campaigns measure the water pressure, which can be used to compute the total or still water level (SWL). In the final offline campaign files provided by Fugro (2024a,b) the water level values are directly available. In the data provided for the verification shown in Deltares (2024) only the water pressure observations are available and we have converted these into water levels. Furthermore, given that water level observations are by nature inhomogeneous, with variations in the location of the sensor generally leading to jumps in the observed levels, in the density scatter comparisons shown the monthly bias between the model and the observations has been removed. Also due to the inhomogeneous nature of the water level observations, the final quality assured dataset can differ significantly from the monthly datasets delivered during the campaign. Because of this, in the comparisons we also plot the observation data considered in Deltares (2024).

5.2 KFII-1 water levels

Figure 5-1 shows the timeseries comparisons between the total water level model results and observations from KFII-1-LB and KFII-1-CP. The respective density scatter comparisons are given in Figure 5-2 (KFII-1-LB) and Figure 5-3 (KFII-1-CP). As noted, because the final campaign data can significantly differ from the monthly data considered in Deltares (2024), the timeseries plots also include the data considered in Deltares (2024), the grey lines in the figures, and the density scatter plots between the model results and the data considered in Deltares (2024) are also given in the top row of the density scatter figures. All figures show a high correspondence between the model results and the KFII-1 observations and that the quality of model results is equally high in all considered campaign periods.

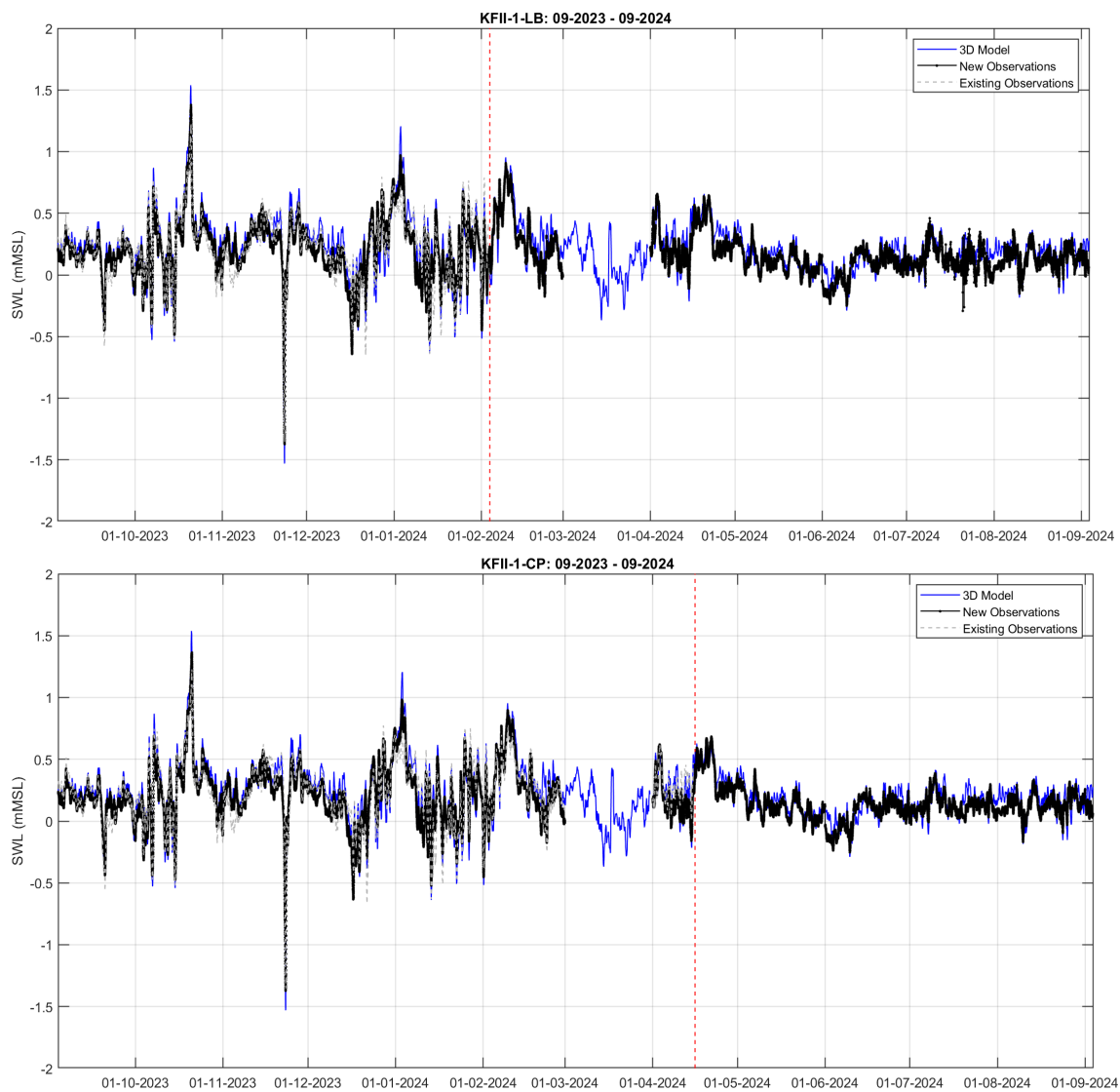


Figure 5-1 Timeseries comparisons between the calibrated model results and the observations from KFII-1-LB (top) and KFII-1-CP (bottom) of total water level.

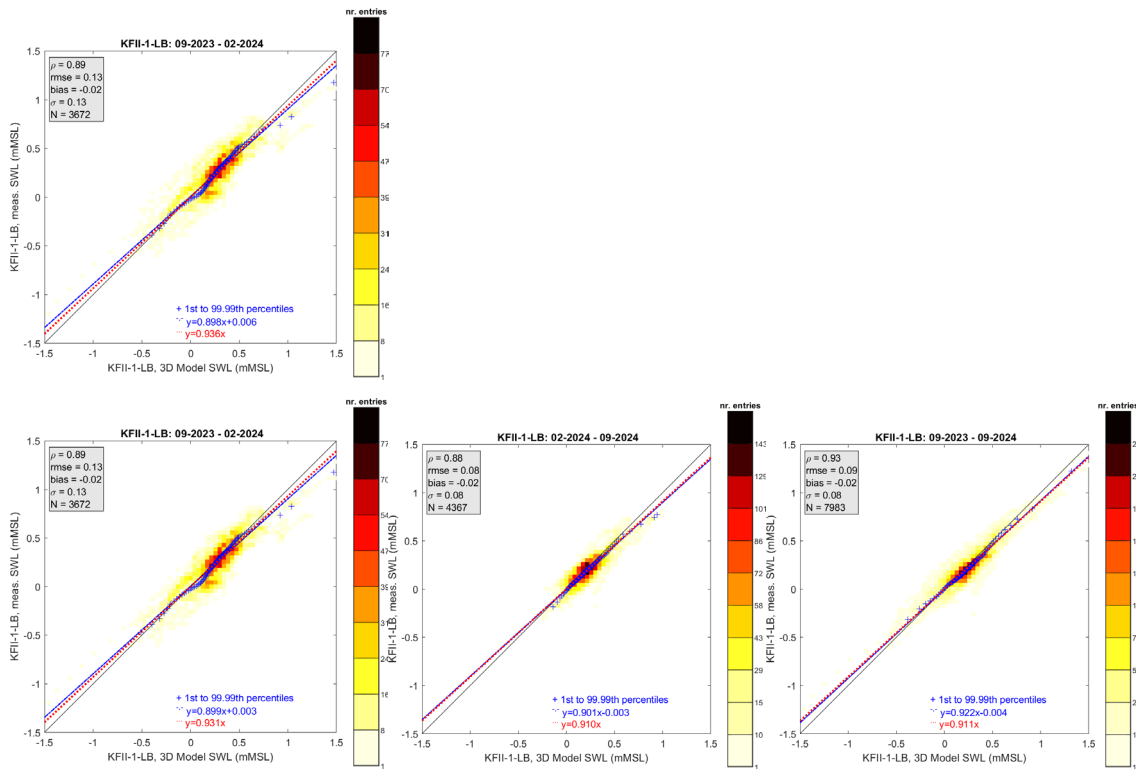


Figure 5-2 Density scatter comparisons between the calibrated model results and the observations from KFII-1-LB water level. The plot in the top row is for the observations received during the study, the plots in the bottom row are for the final campaign observations. The periods covered by the data are 09-2023 to 02-2024 (left column), 02-2024 to 09-2024 (middle column) and 09-2023 to 09-2024 (right column).

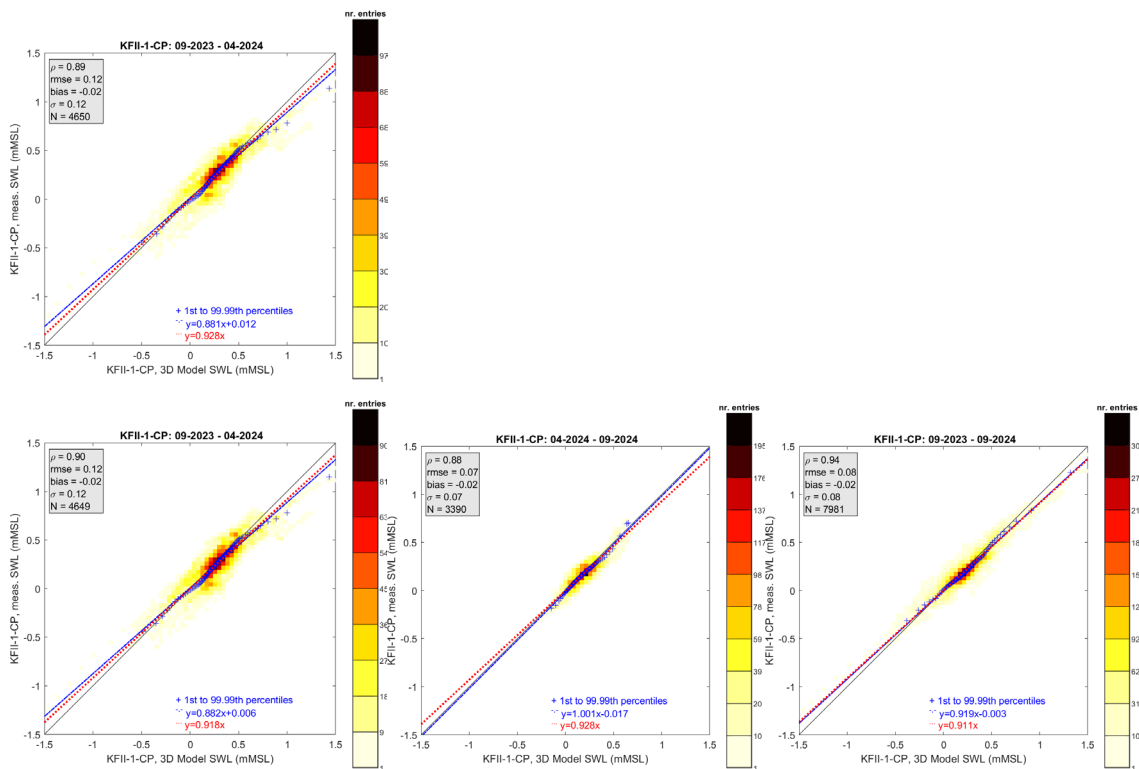


Figure 5-3 Density scatter comparisons between the calibrated model results and the observations from KFII-1-CP water level. The plot in the top row is for the observations received during the study, the plots in the bottom row are for the final campaign observations. The periods covered by the data are 09-2023 to 04-2024 (left column), 04-2024 to 09-2024 (middle column) and 09-2023 to 09-2024 (right column).

5.3 KFII-2 water levels

Figure 5-4 shows the timeseries comparisons between the total water level model results and observations from KFII-2-LB and KFII-2-CP. The respective density scatter comparisons are given in Figure 5-5 (KFII-2-LB) and Figure 5-6 (KFII-2-CP). All figures show a high correspondence between the model results and the KFII-2 observations and that the quality of model results is equally high in all considered campaign periods.

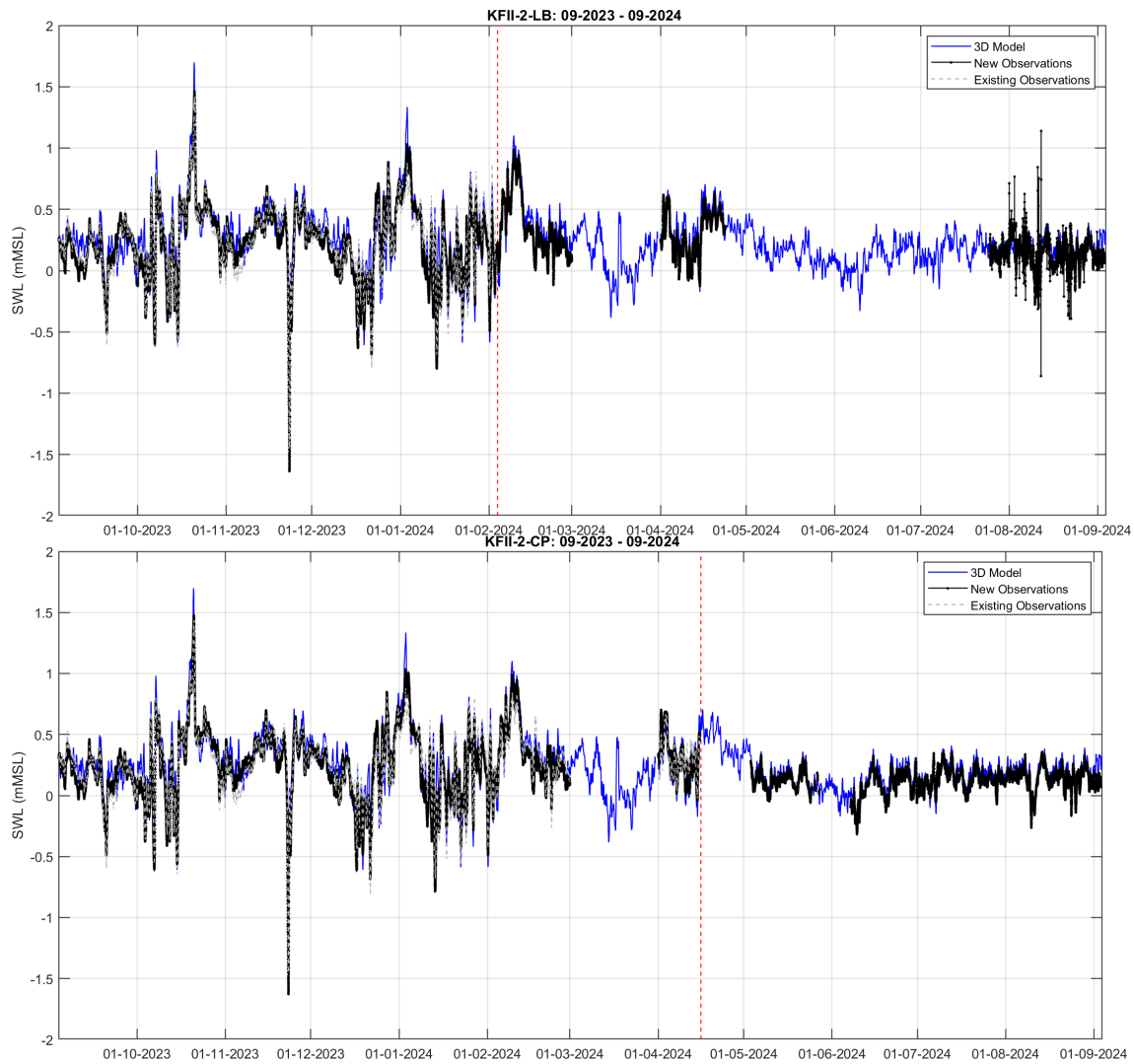


Figure 5-4 Timeseries comparisons between the calibrated model results and the observations from KFII-2-LB (top) and KFII-2-CP (bottom) of total water level.

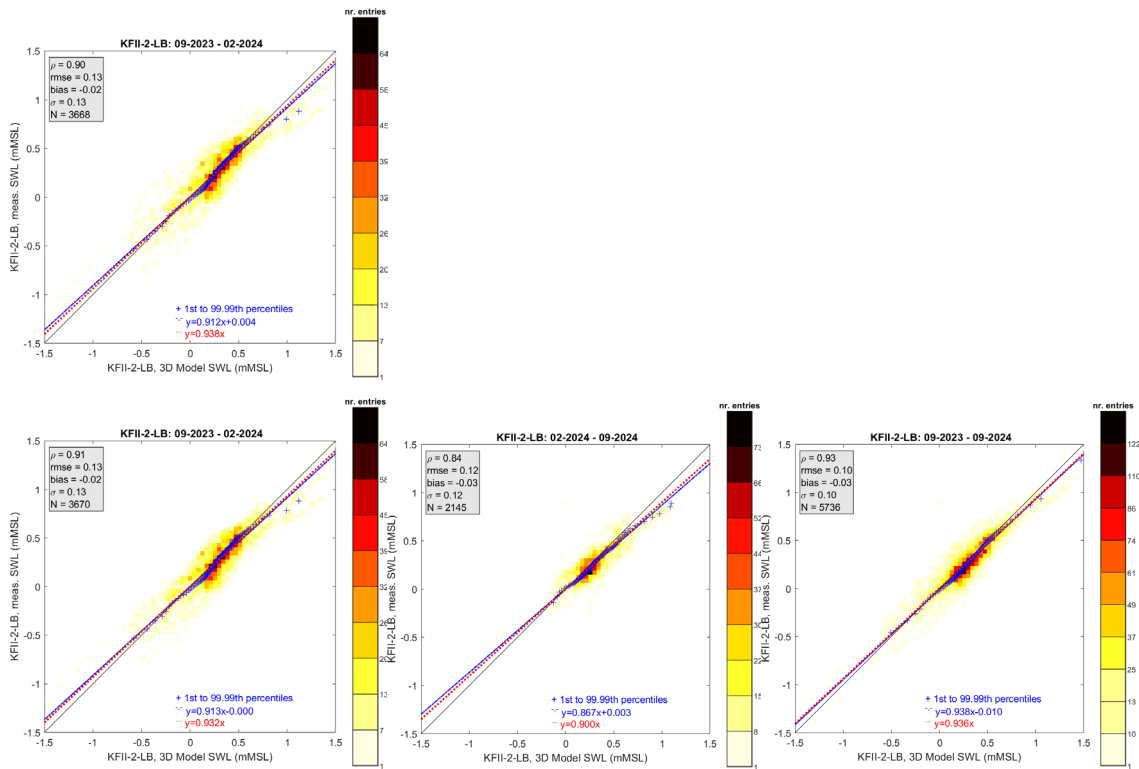


Figure 5-5 Density scatter comparisons between the calibrated model results and the observations from KFII-2-LB water level. The plot in the top row is for the observations received during the study, the plots in the bottom row are for the final campaign observations. The periods covered by the data are 09-2023 to 02-2024 (left column), 02-2024 to 09-2024 (middle column) and 09-2023 to 09-2024 (right column).

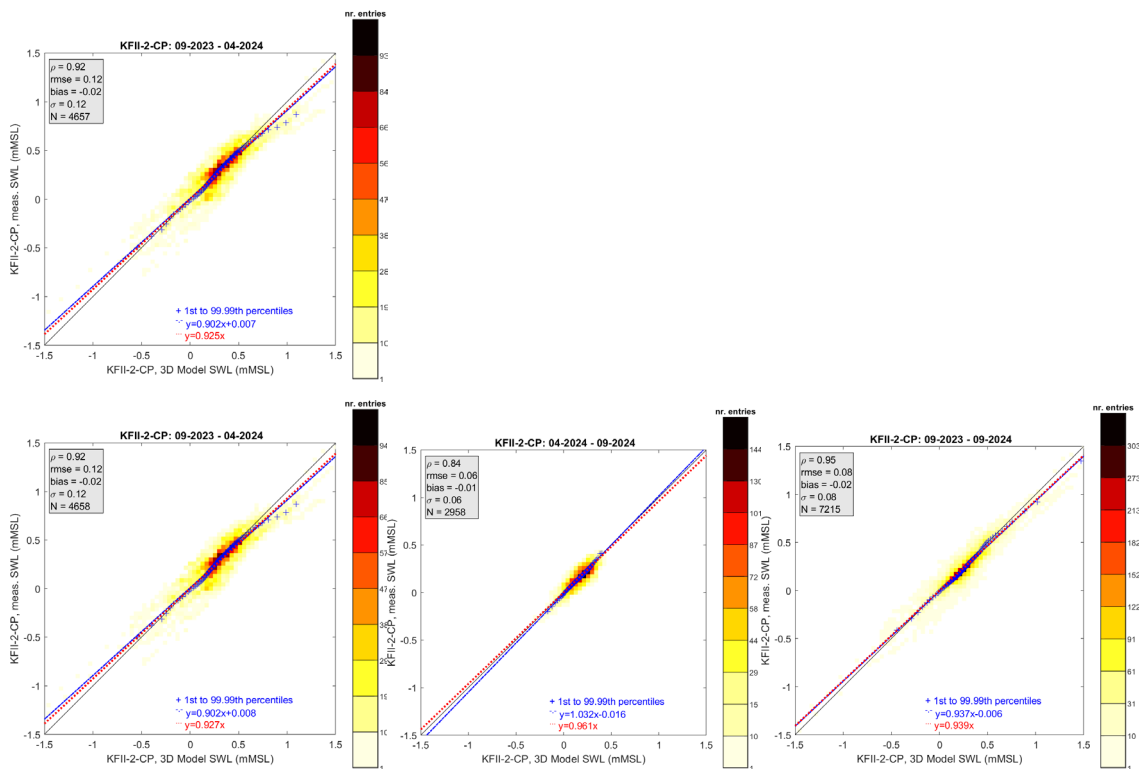


Figure 5-6 Density scatter comparisons between the calibrated model results and the observations from KFII-2-LB water level. The plot in the top row is for the observations received during the study, the plots in the bottom row are for the final campaign observations. The periods covered by the data are 09-2023 to 04-2024 (left column), 04-2024 to 09-2024 (middle column) and 09-2023 to 09-2024 (right column).

5.4 KFII-3 water levels

Figure 5-7 (Figure 5-8) shows the timeseries (density scatter) comparisons between the total water level model results and observations from KFII-3-LB. Given that the KFII-3-LB data have not been considered in Deltares (2024) the density scatter comparisons in Figure 5-8 are only for the full campaign period, from November 2023 until April 2024. The figures show that as for the observations from KFII-1 and KFII-2, the agreement between the model results and the observations is high, confirming the validity of the model results.

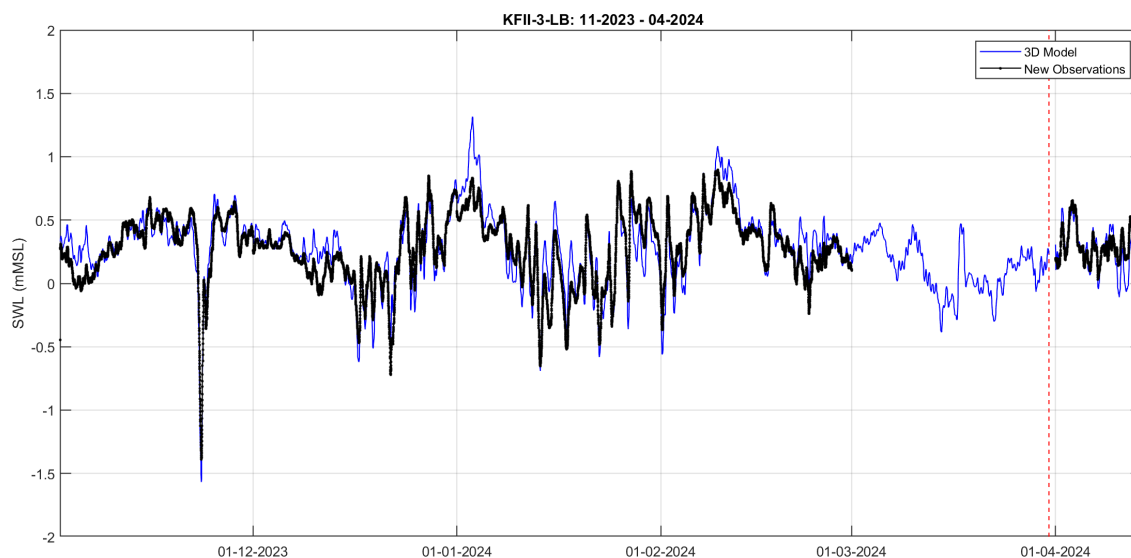


Figure 5-7 Timeseries comparisons between the calibrated model results and the observations from KFII-3-LB of total water level. The vertical red line indicates the end date of the models results in the Deltares (2024) study.

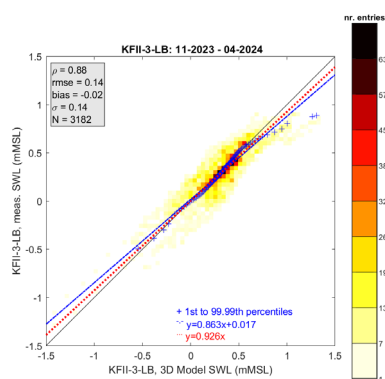


Figure 5-8 Density scatter comparisons between the calibrated model results and the observations from KFII-3-LB water level from 11-2023 until 04-2024.

6 Current reverification

6.1 Introduction

The following sections 6.2, 6.3 and 6.4 show the comparisons between the calibrated model results and the observations from KFII-1, KFII-2 and KFII-3, respectively.

The comparisons are made by means of timeseries and density scatters of depth-averaged current speeds, Hovmöller diagrams of the current speed and average vertical current speed profiles. In the depth-averaged comparisons the model results are integrated across the levels of the respective observations.

Because the current speed observations can contain inhomogeneities due to variations in the location of the sensors, deterioration of the current speed signal due to interferences or contaminations, the final quality assured dataset can differ significantly from the monthly datasets delivered during the campaign. Because of this, as in the water level comparisons, we also show the comparisons with the observation data considered in Deltares (2024).

6.2 KFII-1 currents

Figure 6-1 shows the timeseries comparisons between the depth-averaged current speed model results and observations from KFII-1-LB and KFII-1-CP. The respective density scatter comparisons are given in Figure 6-2 for KFII-1-LB and Figure 6-3 for KFII-1-CP. The figures that the correspondence between the model results and the observations from KFII-1-LB and KFII-1-CP considered in Deltares (2024) and the full campaign data is comparable (cf. top row panel and right panel in the bottom row of Figure 6-2 and Figure 6-3), indicating consistency in the quality of the model results.

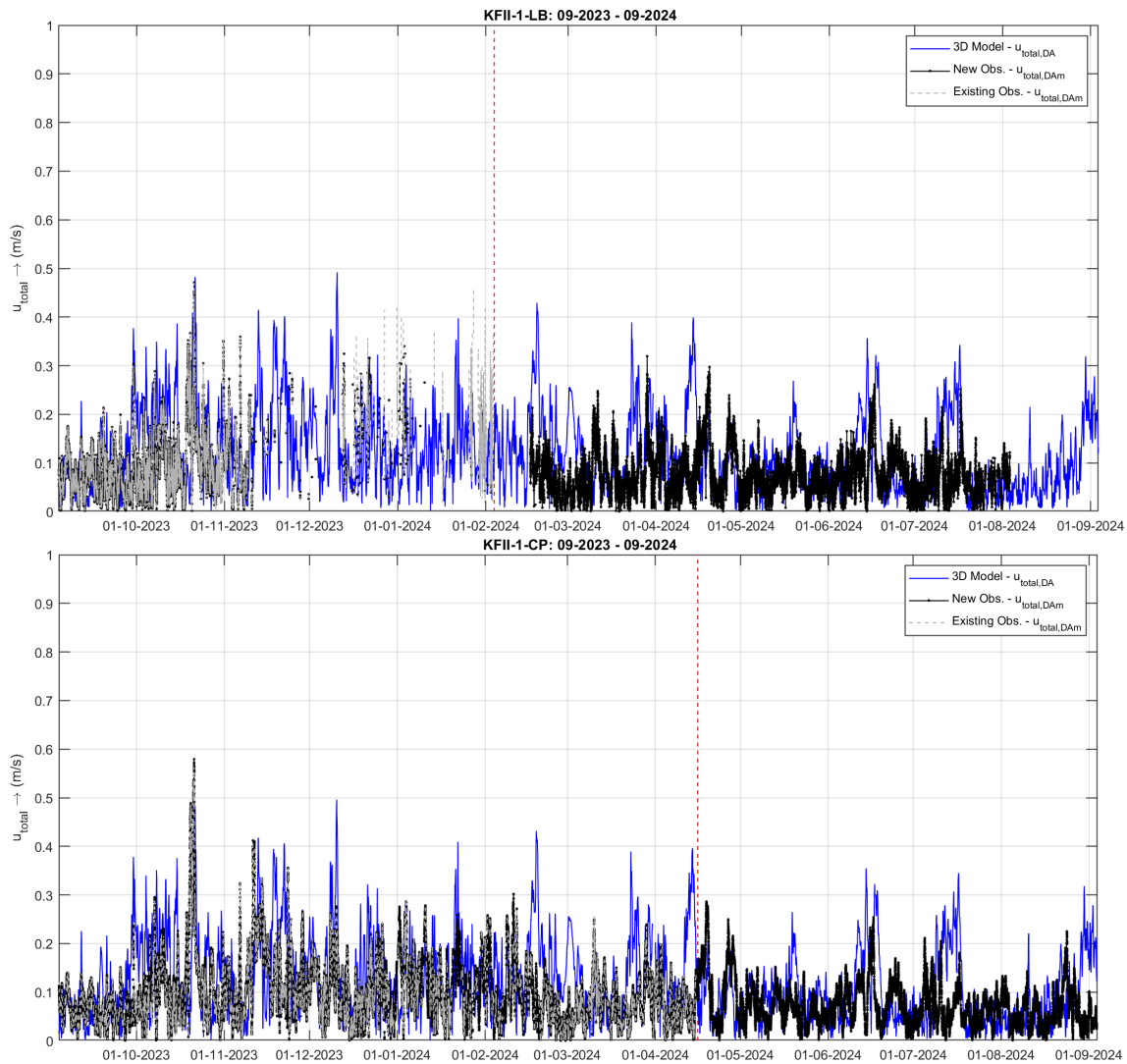


Figure 6-1 Timeseries comparisons between the calibrated model results and the observations from KFII-1-LB (top) KFII-1-CP (bottom) of depth-averaged current speed.

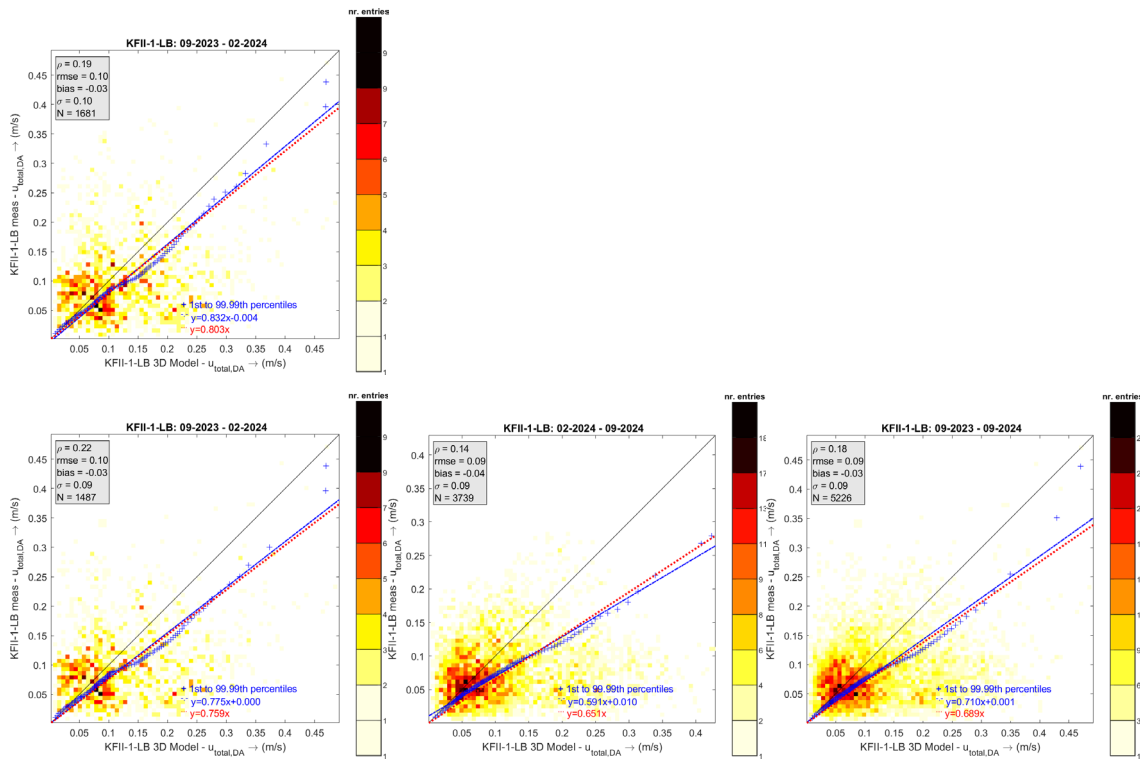


Figure 6-2 Density scatter comparisons between the calibrated model results and the observations from KFII-1-LB of depth-averaged current speed. The plot in the top row is for the observations considered in Deltares (2024), the plots in the bottom row are for the final campaign observations. The periods covered by the data are 09-2023 to 02-2024 (left column), 02-2024 to 09-2024 (middle column) and 09-2023 to 09-2024 (right column).

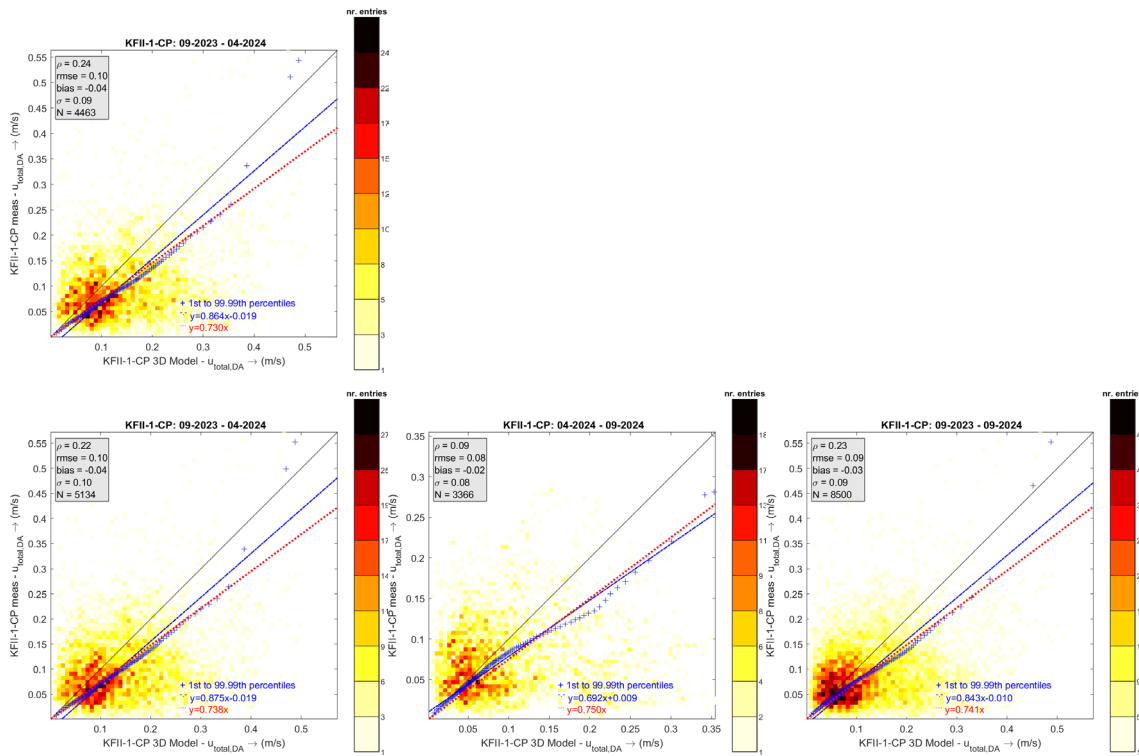


Figure 6-3 Density scatter comparisons between the calibrated model results and the observations from KFII-1-CP of depth-averaged current speed. The plot in the top row is for the observations considered in Deltares (2024), the plots in the bottom row are for the final campaign observations. The periods covered by the data are 09-2023 to 04-2024 (left column), 04-2024 to 09-2024 (middle column) and 09-2023 to 09-2024 (right column).

Figure 6-4 (Figure 6-6) shows the Hovmöller diagrams of the KFII-1-LB (KFII-1-CP) current speed observations considered in Deltares (2024), the final campaign observations and the calibrated 3D model results. Figure 6-5 (Figure 6-7) shows the respective KFII-1-LB (KFII-1-CP) vertical current speed profile plot comparisons. The figures show that the quality of the KFII-1LB observation data considered in Deltares (2024) for the levels closer to the bottom for the deeper level was low and that consequently the correspondence between the vertical profiles of the model results and the observations from KFII-1-LB is higher for the final campaign observations than for the observations considered in Deltares (2024). The correspondence between the vertical profiles of the model results and the final campaign observations from KFII-1-CP is similar in all considered periods and also similar to the correspondence between the vertical profiles of the model results and the observations from KFII-1-CP considered in Deltares (2024).

Based on these, we conclude that the quality of the 3D current model results is consistent throughout the whole KFII-1 campaign period.

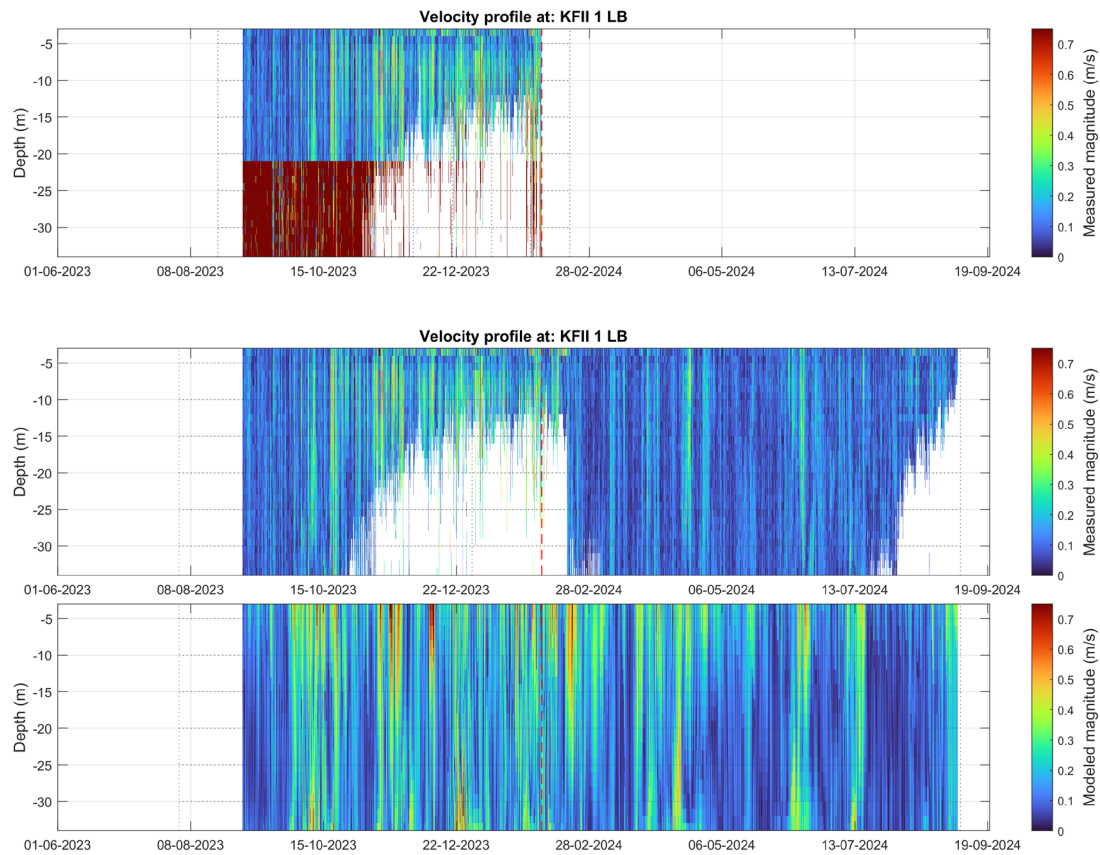


Figure 6-4 Current speed Hovmöller diagrams of the calibrated model results and the observations from KFII-1-LB. The plot in the top row is with the observations considered in Deltares (2024), the plot in the bottom row is with the final campaign observations and the plot in the bottom row is with the model results.

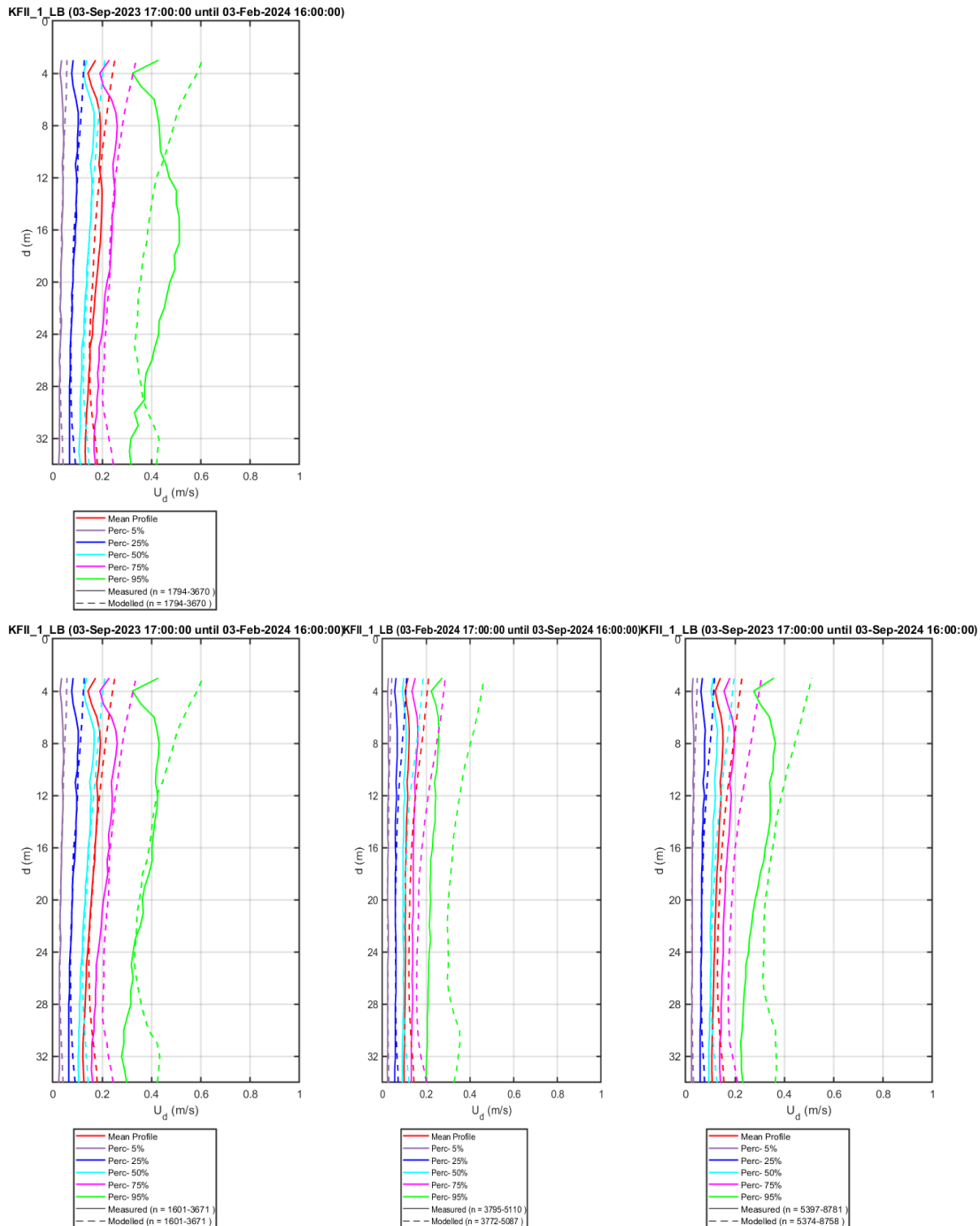


Figure 6-5 Current magnitude 3D profile plots comparisons between the calibrated 3D model results (dashed lines) and the observations (full lines) from KFII-1-LB. The plot in the top row is for the observations considered in Deltares (2024), the plots in the bottom row are for the final campaign observations. The periods covered by the data are 09-2023 to 02-2024 (left column), 02-2024 to 09-2024 (middle column) and 09-2023 to 09-2024 (right column).

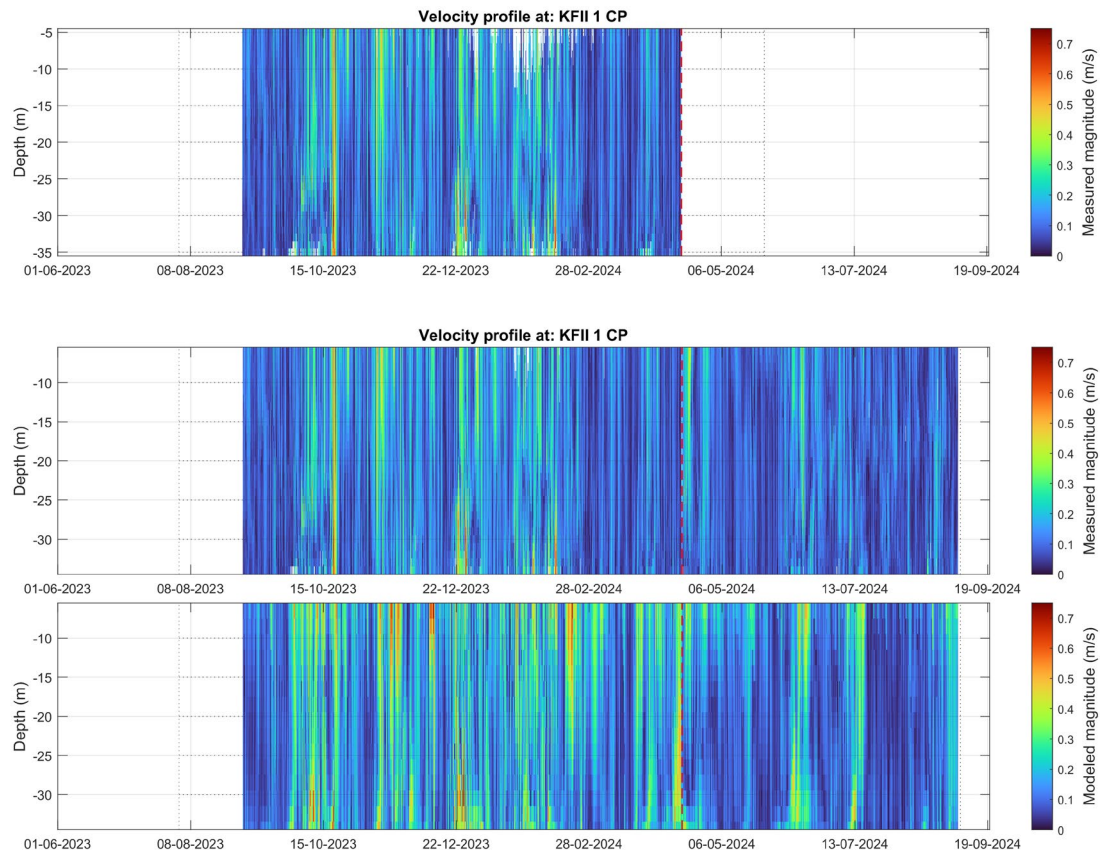


Figure 6-6 Current speed Hovmöller diagrams of the calibrated model results and the observations from KFII-1-CP. The plot in the top row is with the observations considered in Deltares (2024), the plot in the bottom row is with the final campaign observations and the plot in the bottom row is with the model results.

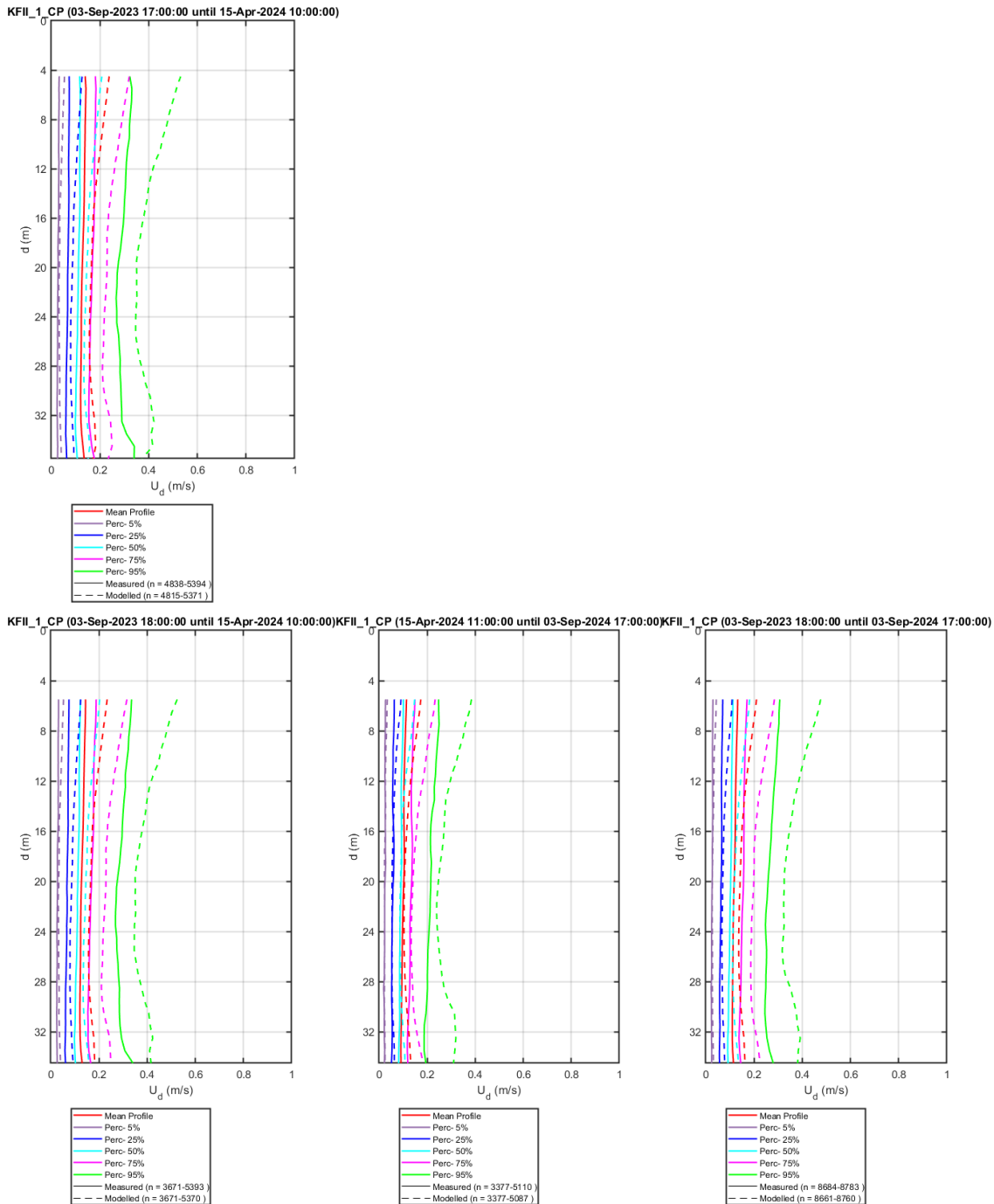


Figure 6-7 Current magnitude 3D profile plots comparisons between the calibrated 3D model results (dashed lines) and the observations (full lines) from KFII-1-CP. The plot in the top row is for the observations considered in Deltares (2024), the plots in the bottom row are for the final campaign observations. The periods covered by the data are 09-2023 to 04-2024 (left column), 04-2024 to 09-2024 (middle column) and 09-2023 to 09-2024 (right column).

6.3 KFII-2 currents

Figure 6-8 shows the timeseries comparisons between the depth-averaged current speed model results and observations from KFII-2-LB and KFII-2-CP. The respective density scatter comparisons are given in Figure 6-9 (KFII-2-LB) and Figure 6-10 (KFII-2-CP). The KFII-2-LB are

only valid in the period considered in Deltares (2024) and the agreement between the model results and the data considered in Deltares (2024) and the final campaign data is the same. The availability of the KFII-2-CP data is higher and Figure 6-10 shows that the correspondence between the model results and the observations from KFII-2-CP considered in Deltares (2024) and the full campaign data is comparable (cf. top row panel and right panel in the bottom row of Figure 6-10), indicating consistency in the quality of the model results.

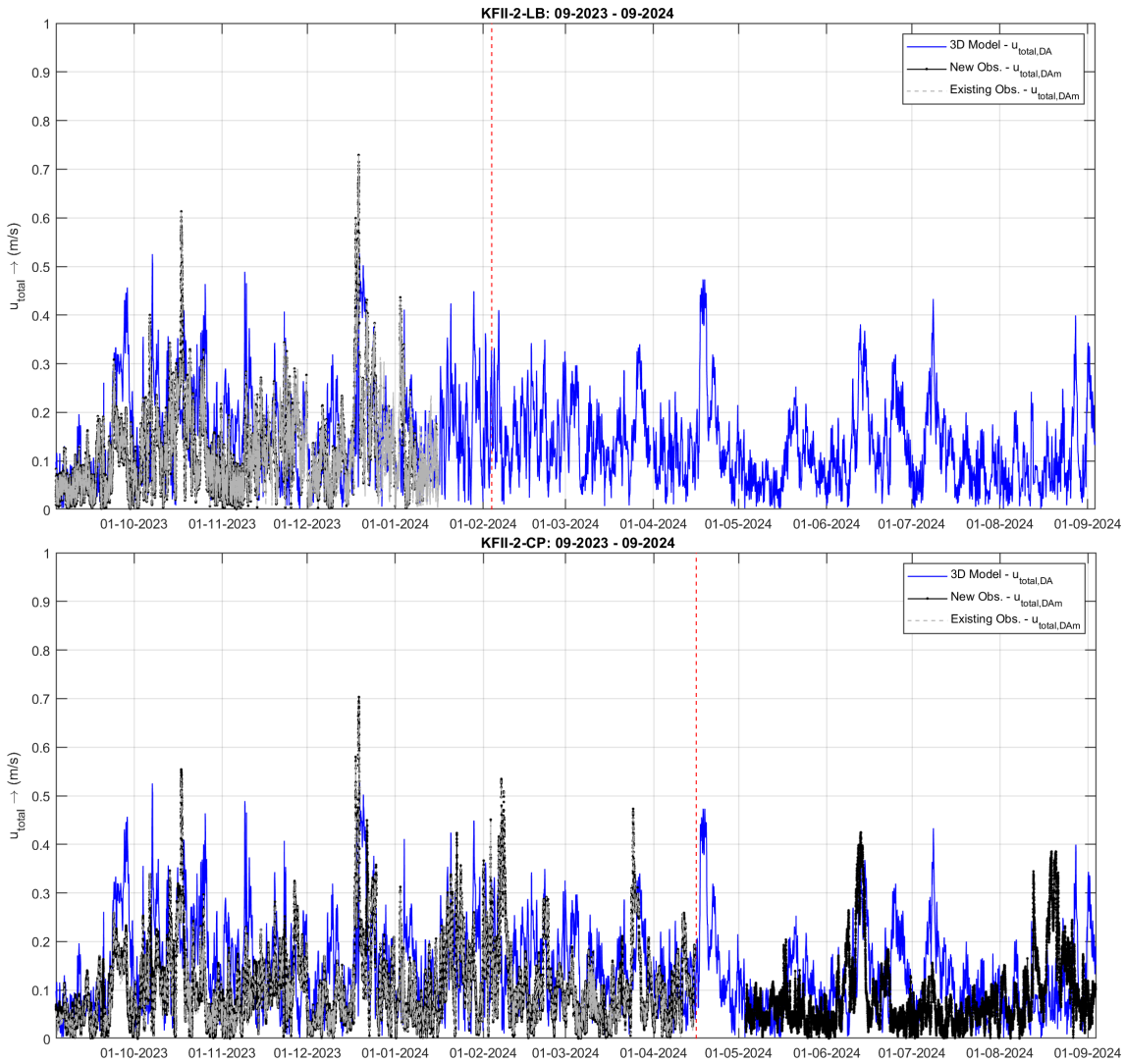


Figure 6-8 Timeseries comparisons between the calibrated model results and the observations from KFII-2-LB of depth-averaged current speed.

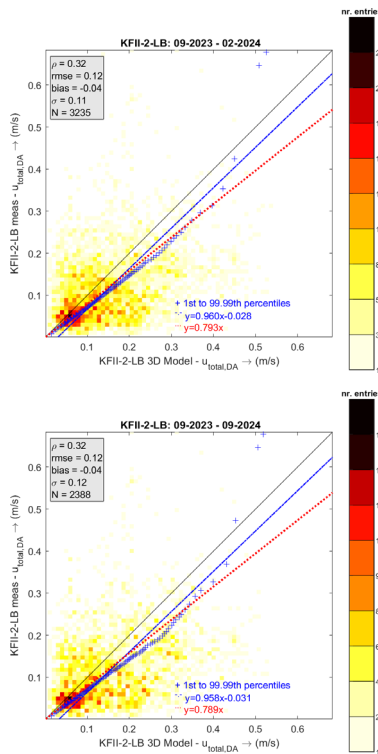


Figure 6-9 Density scatter comparisons between the calibrated model results and the observations from KFII-2-LB of depth-averaged current speed. The plot in the top row is for the observations considered in Deltares (2024), the plots in the bottom row are for the final campaign observations. The final campaign data contains no valid data outside the period considered in Deltares (2024).

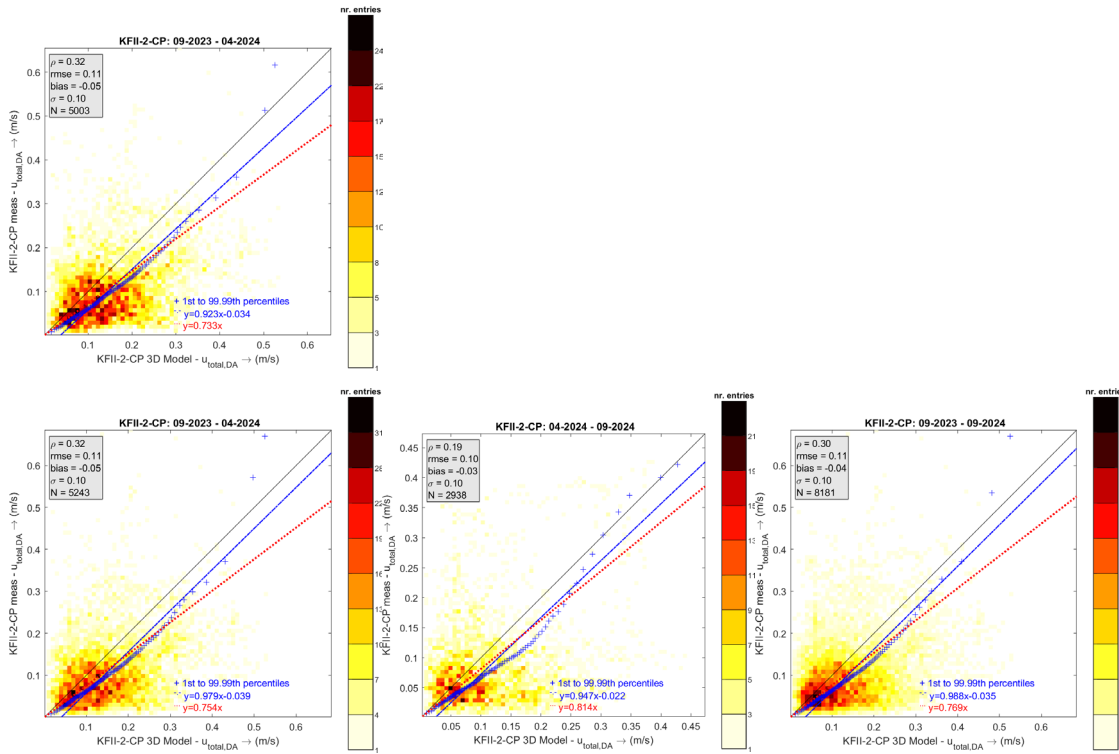


Figure 6-10 Density scatter comparisons between the calibrated model results and the observations from KFII-2-CP of depth-averaged current speed. The plot in the top row is for the observations considered in Deltares (2024), the plots in the bottom row are for the final campaign observations. The periods covered by the data are 09-2023 to 04-2024 (left column), 04-2024 to 09-2024 (middle column) and 09-2023 to 09-2024 (right column).

Figure 6-11 (Figure 6-13) shows the Hovmöller diagrams of the KFII-2-LB (KFII-2-CP) current speed observations considered in Deltares (2024), the final campaign observations and the calibrated 3D model results. Figure 6-12 (Figure 6-14) shows the respective KFII-2-LB (KFII-2-CP) vertical current speed profile plot comparisons. The figures show that the quality of the KFII-2-LB observation data considered in Deltares (2024) for the levels closer to the bottom is lower than the final campaign data. Nevertheless, the correspondence between the vertical profiles of the model results and observations considered in Deltares (2024) and the final campaign observations is comparable. Furthermore, as also noted in terms of depth-average speeds, the correspondence between the model results and the observations from KFII-2-CP considered in Deltares (2024) and the full campaign data is comparable, indicating consistency in the quality of the model results.

Based on these, we conclude that the quality of the 3D current model results is consistent throughout the whole KFII-2 campaign period.

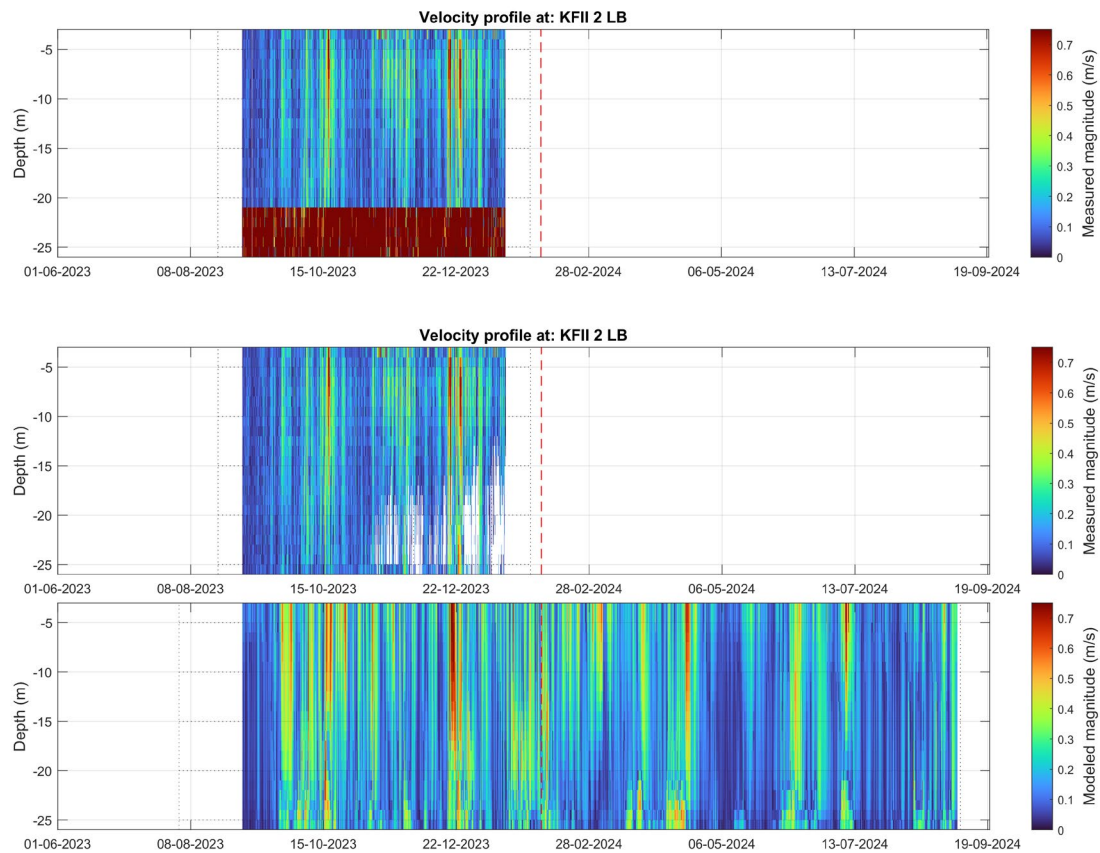
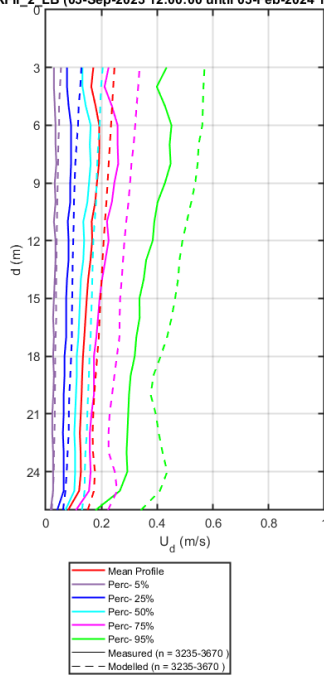


Figure 6-11 Current speed Hovmöller diagrams of the calibrated model results and the observations from KFII-2-LB. The plot in the top row is with the observations considered in Deltares (2024), the plot in the bottom row is with the final campaign observations and the plot in the bottom row is with the model results.

KFII_2_LB (03-Sep-2023 12:00:00 until 03-Feb-2024 11:00:00)



KFII_2_LB (03-Sep-2023 12:00:00 until 03-Sep-2024 11:00:00)

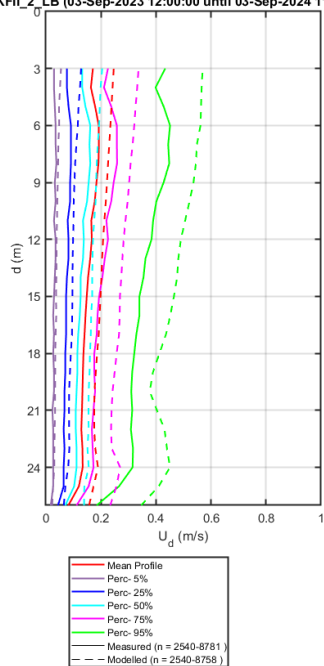


Figure 6-12 Current magnitude 3D profile plots comparisons between the calibrated 3D model results (dashed lines) and the observations (full lines) from KFII-2-LB. The plot in the top row is for the observations considered in Deltares (2024), the plots in the bottom row are for the final campaign observations. The final campaign data contains no valid data outside the period considered in Deltares (2024).

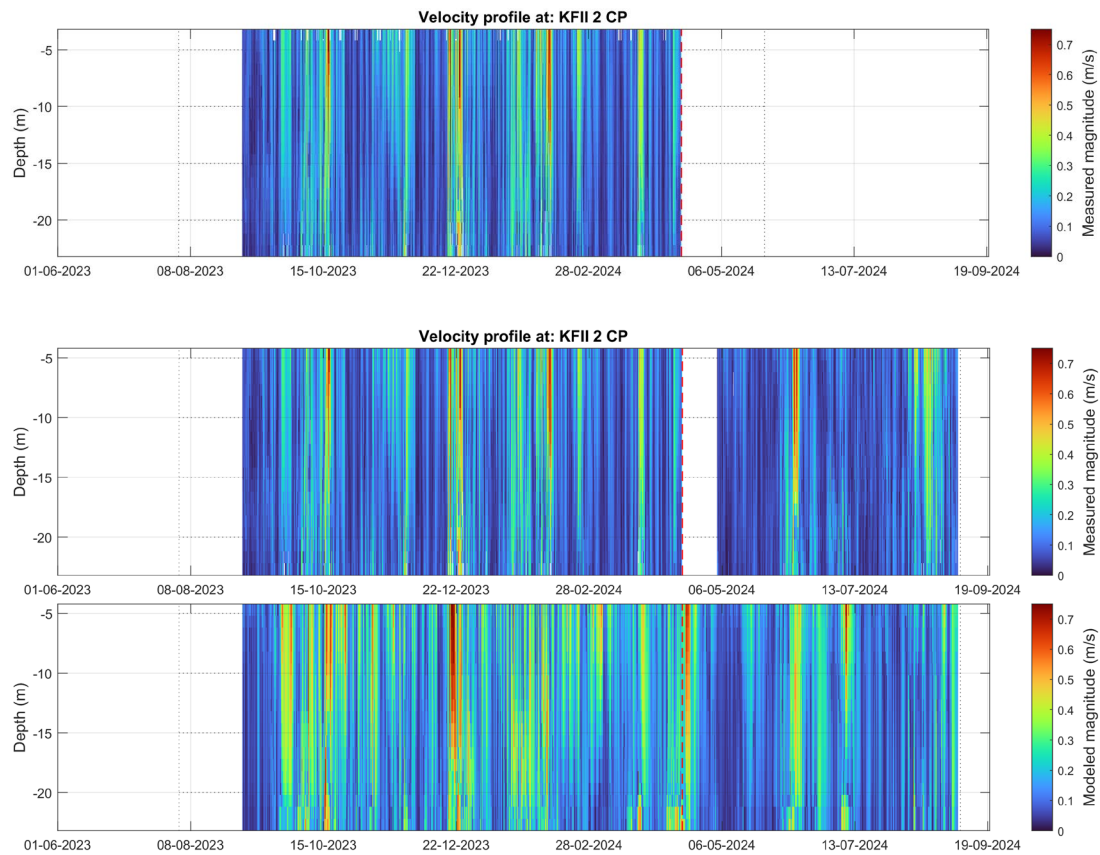


Figure 6-13 Current speed Hovmöller diagrams of the calibrated model results and the observations from KFII-2-CP. The plot in the top row is with the observations considered in Deltares (2024), the plot in the bottom row is with the final campaign observations and the plot in the bottom row is with the model results.

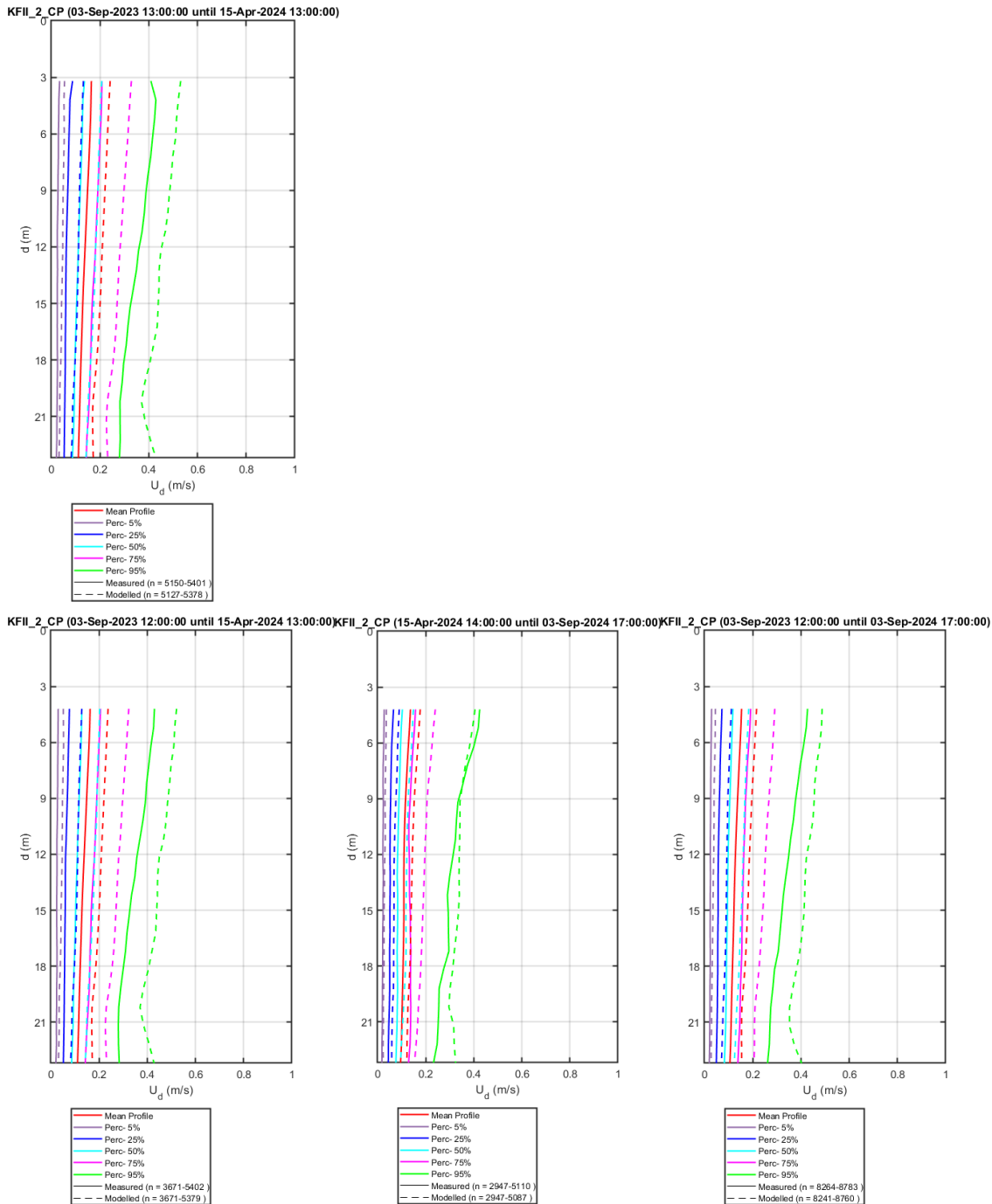


Figure 6-14 Current magnitude 3D profile plots comparisons between the calibrated 3D model results (dashed lines) and the observations (full lines) from KFII-2-CP. The plot in the top row is for the observations considered in Deltares (2024), the plots in the bottom row are for the final campaign observations. The periods covered by the data are 09-2023 to 04-2024 (left column), 04-2024 to 09-2024 (middle column) and 09-2023 to 09-2024 (right column).

6.4 KFII-3 currents

Figure 6-15, Figure 6-16, Figure 6-17 and Figure 6-18 show respectively the depth-averaged current speed timeseries, depth-averaged current speed density scatter, Hovmöller diagrams and vertical current speed profile comparisons between the model results and observations

from KFII-3-LB. In the all figures the comparisons are only for the full observation period as the KFII-3 data have not been considered in Deltares (2024). The figures show that the correspondence between the model results and the KFII-3 observations is similar to that between model results and the KFII-1 and KFII-2 observations, with the model results generally overestimating the observations. This is an indication that the quality of the data in KFII-3 is comparable with the quality of the data assessed in Deltares (2024). Based on these, we conclude that quality of the basis current data is as reported in Deltares (2024) and there is no need for recalibration.

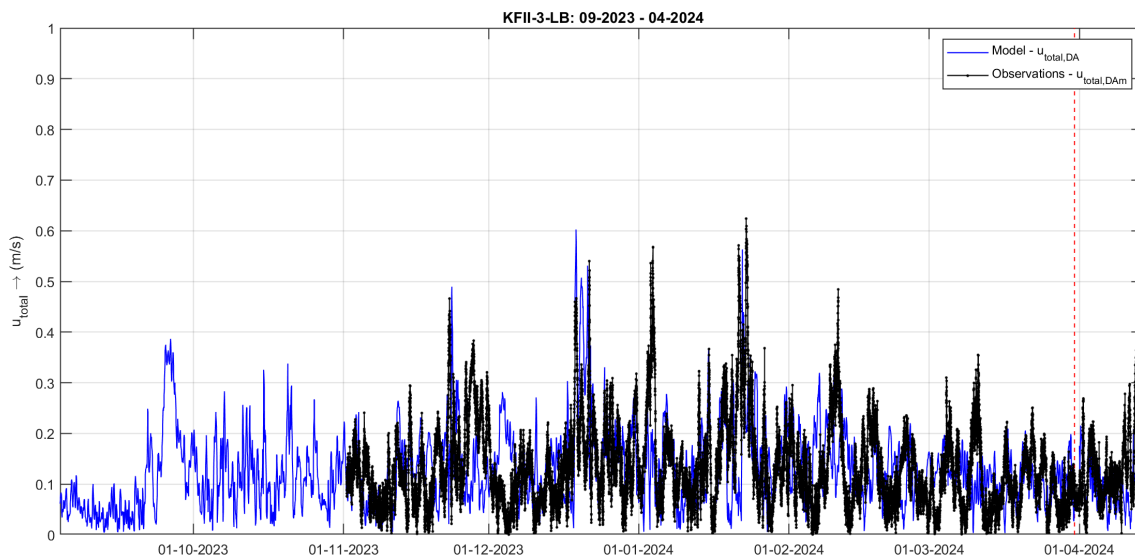


Figure 6-15 Timeseries comparisons between the calibrated model results and the observations from KFII-3-LB of depth-averaged current speed. The vertical red line indicates the end date of the models results in the Deltares (2024) study.

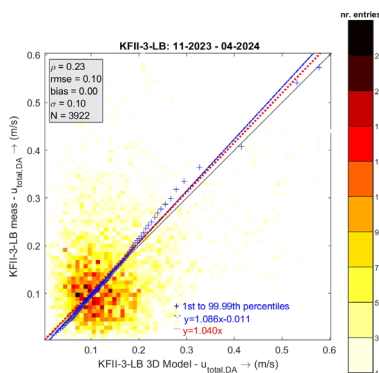


Figure 6-16 Density scatter comparisons between the calibrated model results and the observations from KFII-3-LB of depth-averaged current from 11-2023 to 04-2024.

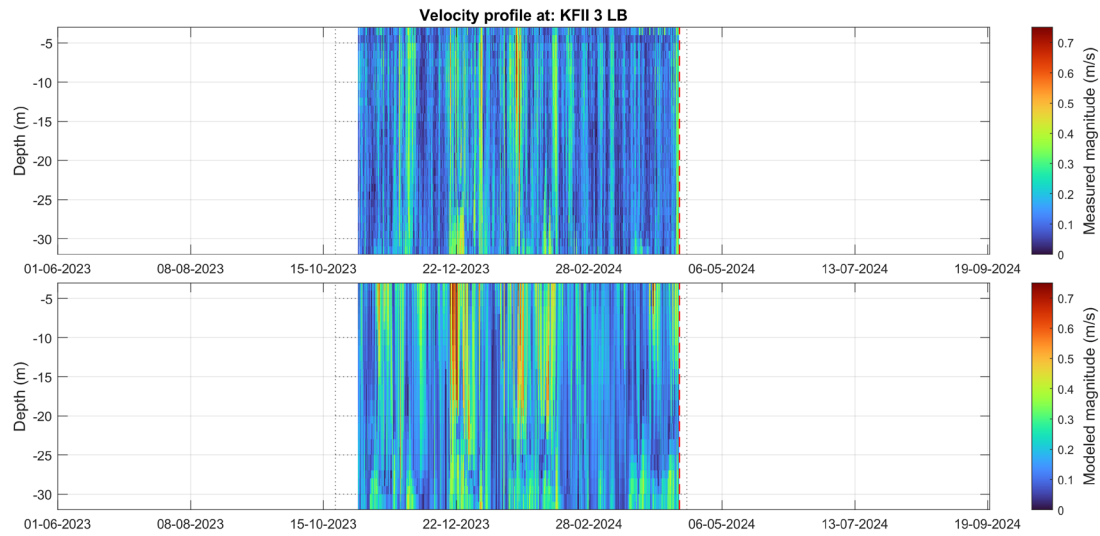


Figure 6-17 Current speed Hovmöller diagrams of the observations (top panel) and the calibrated model results (bottom panel) from KFII-3-CP.

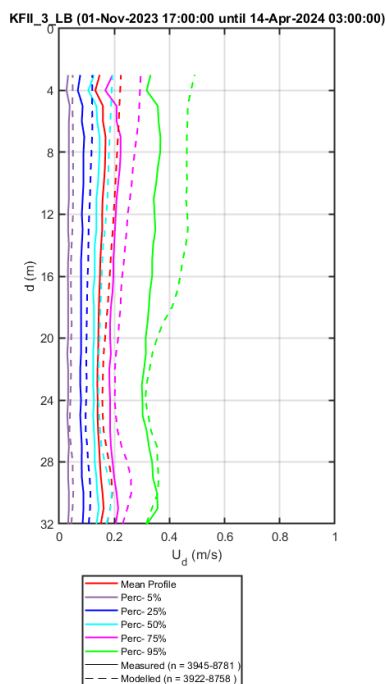


Figure 6-18 Current magnitude 3D profile plots comparisons between the calibrated 3D model results (dashed lines) and the observations (full lines) from KFII-3-LB from 11-2023 to 04-2024.

7 Temperature reverification

The validation of thermodynamic parameters was performed in Deltares (2024) using near-bottom temperature observations from KFII-1-CP and KFII-2-CP and near-surface temperature observations from KFII-1-LB and KFII-2-LB. The final campaign datasets (Fugro, 2024a,b) contain extra data from KFII-1-LB, KFII-1-CP and KFII-2-CP and new near-surface temperature observations from KFII-3-LB. Figure 7-1, Figure 7-2, and Figure 7-3 show the comparisons at KFII-1, KFII-2 and KFII-3 respectively, considering the observations from the full campaign period (Fugro, 2024a,b). The figures show that there is a general agreement between the model results and the observations in both periods, indicating that the assessed validity of thermodynamic model data in Deltares (2024) still holds.

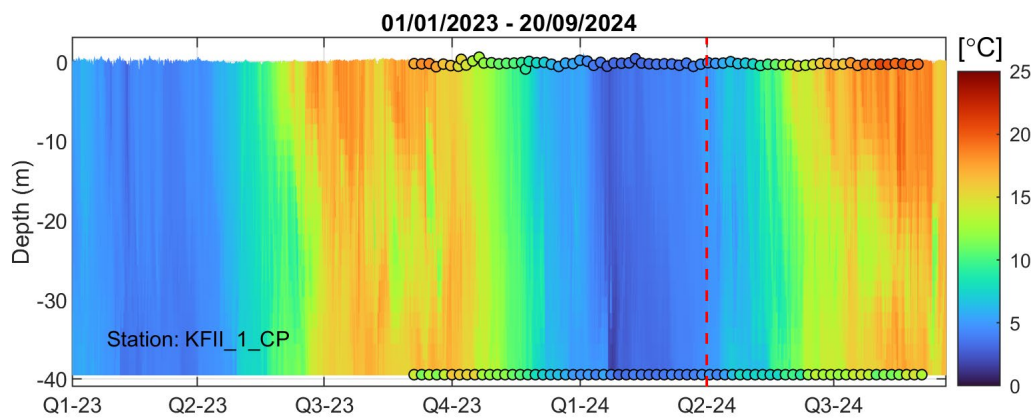


Figure 7-1 Hovmöller diagrams of the 3D temperature model results (background colour map) and near-bottom and near-surface temperature observations (coloured circles) from KFII-1-CP and KFII-1-LB, respectively. The vertical line indicates the date until which the observation data have been considered in the Deltares (2024).

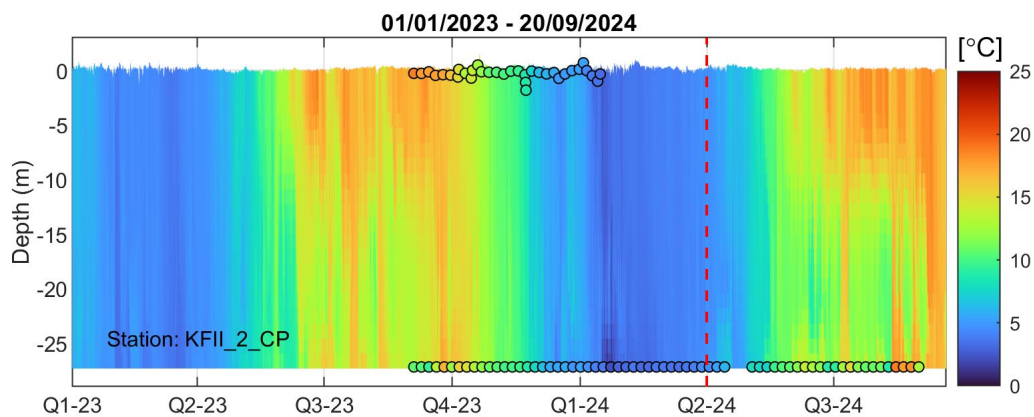


Figure 7-2 Hovmöller diagrams of the 3D temperature model results (background colour map) and near-bottom and near-surface temperature observations (coloured circles) from KFII-2-CP and KFII-2-LB, respectively. The vertical line indicates the date until which the observation data have been considered in the Deltares (2024).

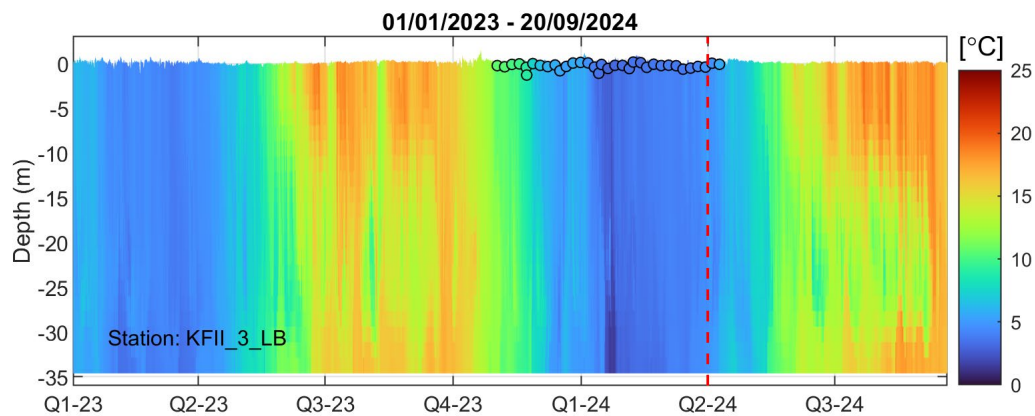


Figure 7-3 Hovmöller diagrams of the 3D temperature model results (background colour map) and near-surface temperature observations (coloured circles) from KFII-3-LB. The vertical line indicates the date until which the observation data have been considered in the Deltares (2024).

8 Wave reverification

8.1 Introduction

The following sections 8.2, 8.3 and 8.4 show the comparisons between the calibrated model results and the observations of significant wave height (H_s), peak wave period (T_p) and mean wave direction (MWD) from KFII-1, KFII-2 and KFII-3, respectively.

8.2 KFII-1 waves

Figure 8-1 shows the timeseries comparisons between the model results and the observations of H_s , T_p and MWD at KFII-1-LB. The respective density scatter comparisons are given in Figure 8-2. The figures show that the correspondence between the model results and the KFII-1-LB observations is similar in the considered periods, with comparable correlation and fit coefficients. It is, therefore, concluded that the quality of the wave model data is consistent throughout the whole KFII-1 campaign period.

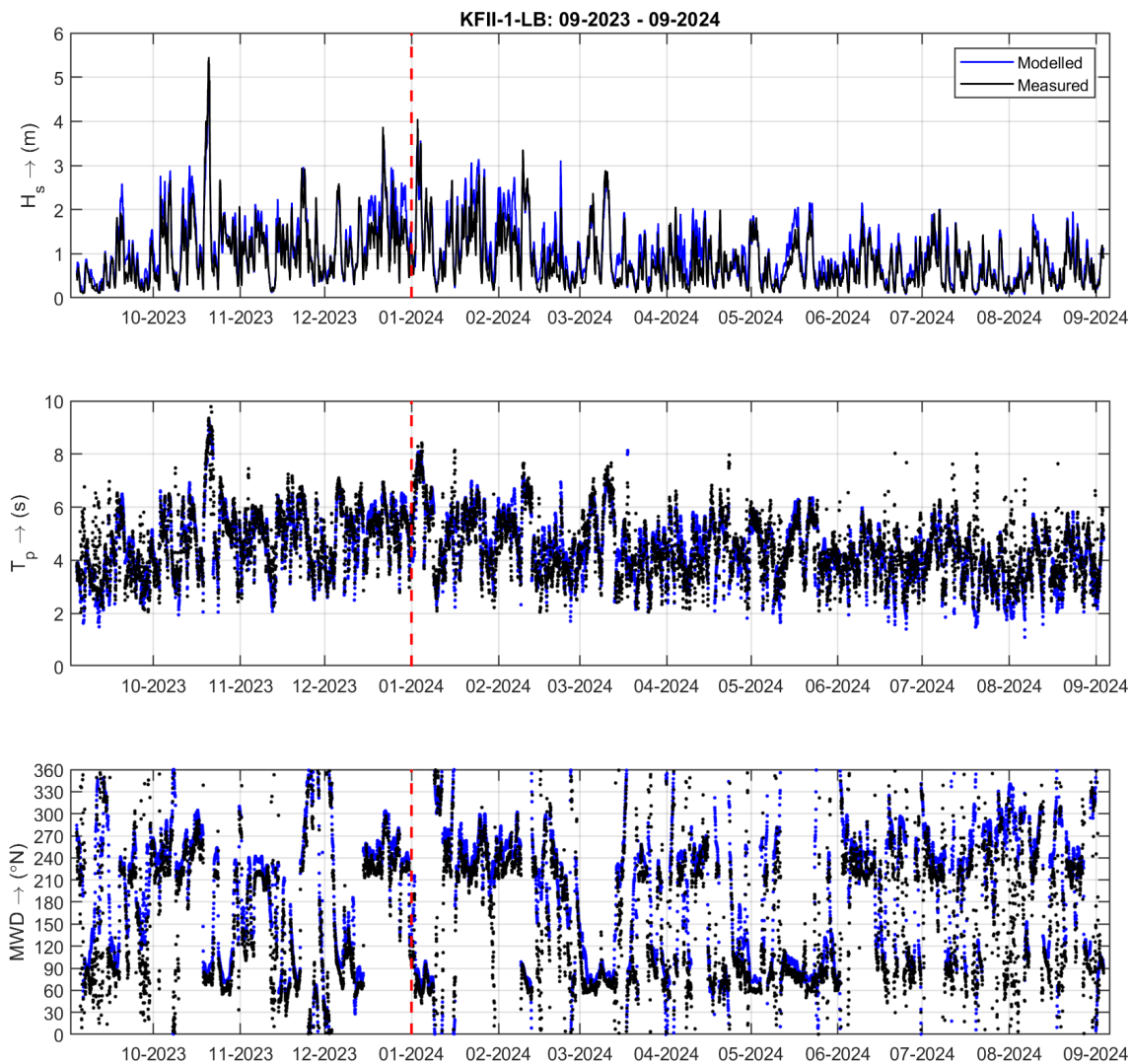


Figure 8-1 Timeseries comparisons between the calibrated model results and the observations from KFII-1-LB of significant wave height (top panel), peak wave period (middle panel) and mean wave direction (bottom panel). The vertical line indicates the date until which the observation data have been considered in the Deltares (2024).

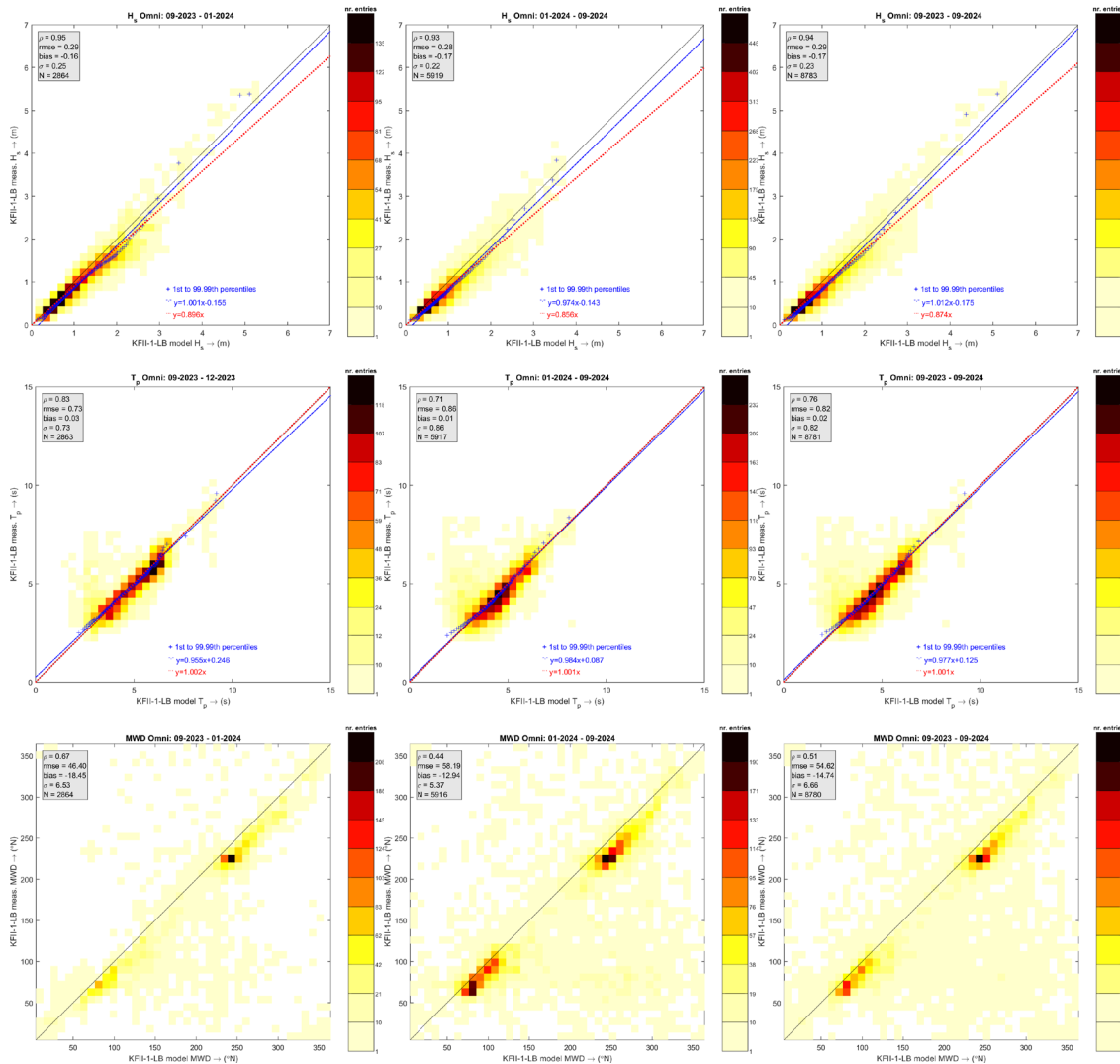


Figure 8-2 Density scatter comparisons between the calibrated model results and the observations from KFII-1-LB of significant wave height (top row), peak wave period (middle row) and mean wave direction (bottom row). The periods covered by the data are 09-2023 to 12-2023 (left column), 01-2024 to 09-2024 (middle column) and 09-2023 to 09-2024 (right column).

8.3 KFII-2 waves

Figure 8-3 shows the timeseries comparisons between the model results and the observations of H_s , T_p and MWD at KFII-2-LB. The respective density scatter comparisons are given Figure 8-4. The figures show that the correspondence between the model results and the KFII-2-LB observations is similar in the considered periods, with comparable correlation and fit coefficients. It is, therefore, concluded that the quality of the wave model data is consistent throughout the whole KFII-2 campaign period.

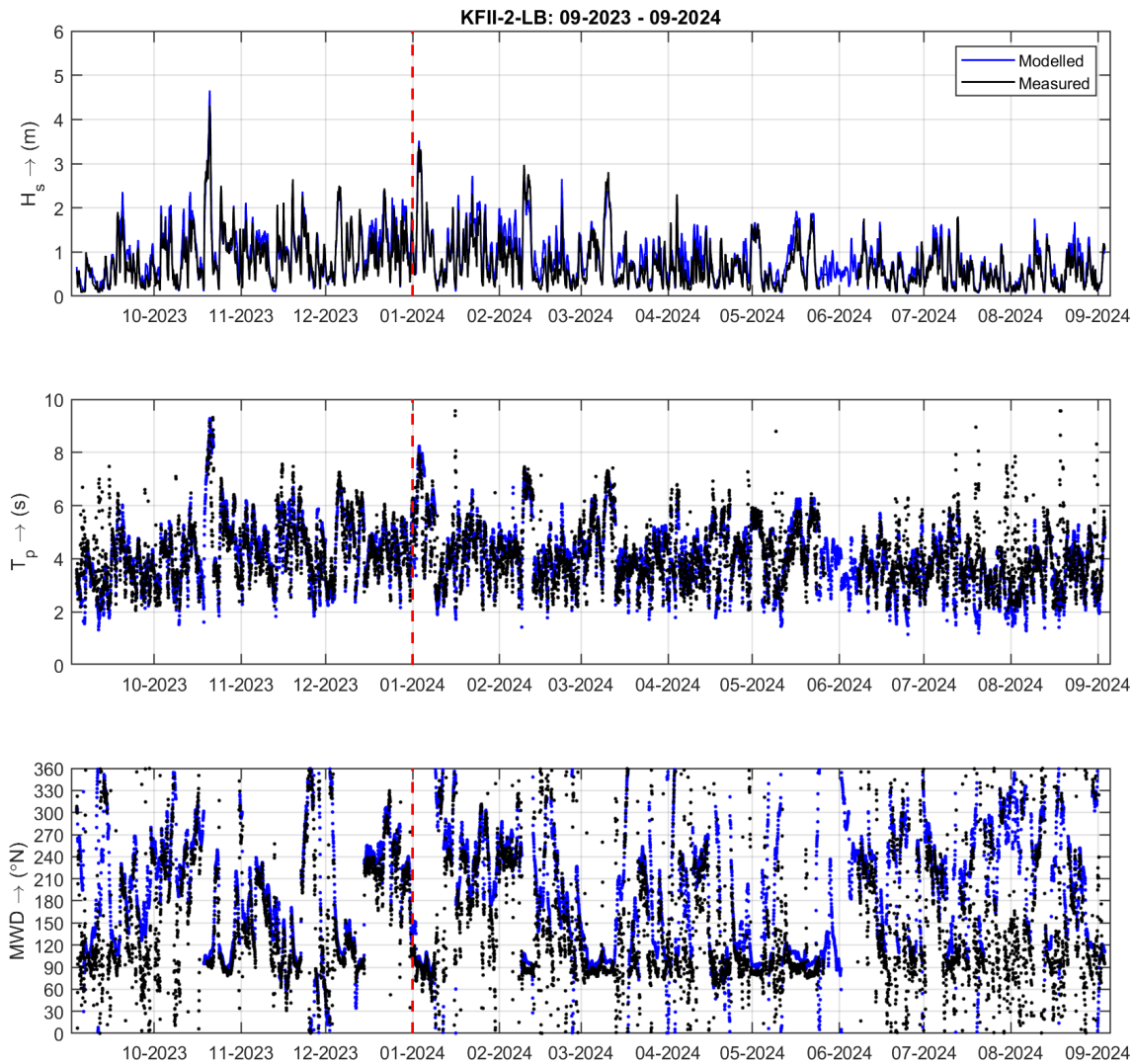


Figure 8-3 Timeseries comparisons between the calibrated model results and the observations from KFII-2-LB of significant wave height (top panel), peak wave period (middle panel) and mean wave direction (bottom panel). The vertical line indicates the date until which the observation data have been considered in the Deltares (2024).

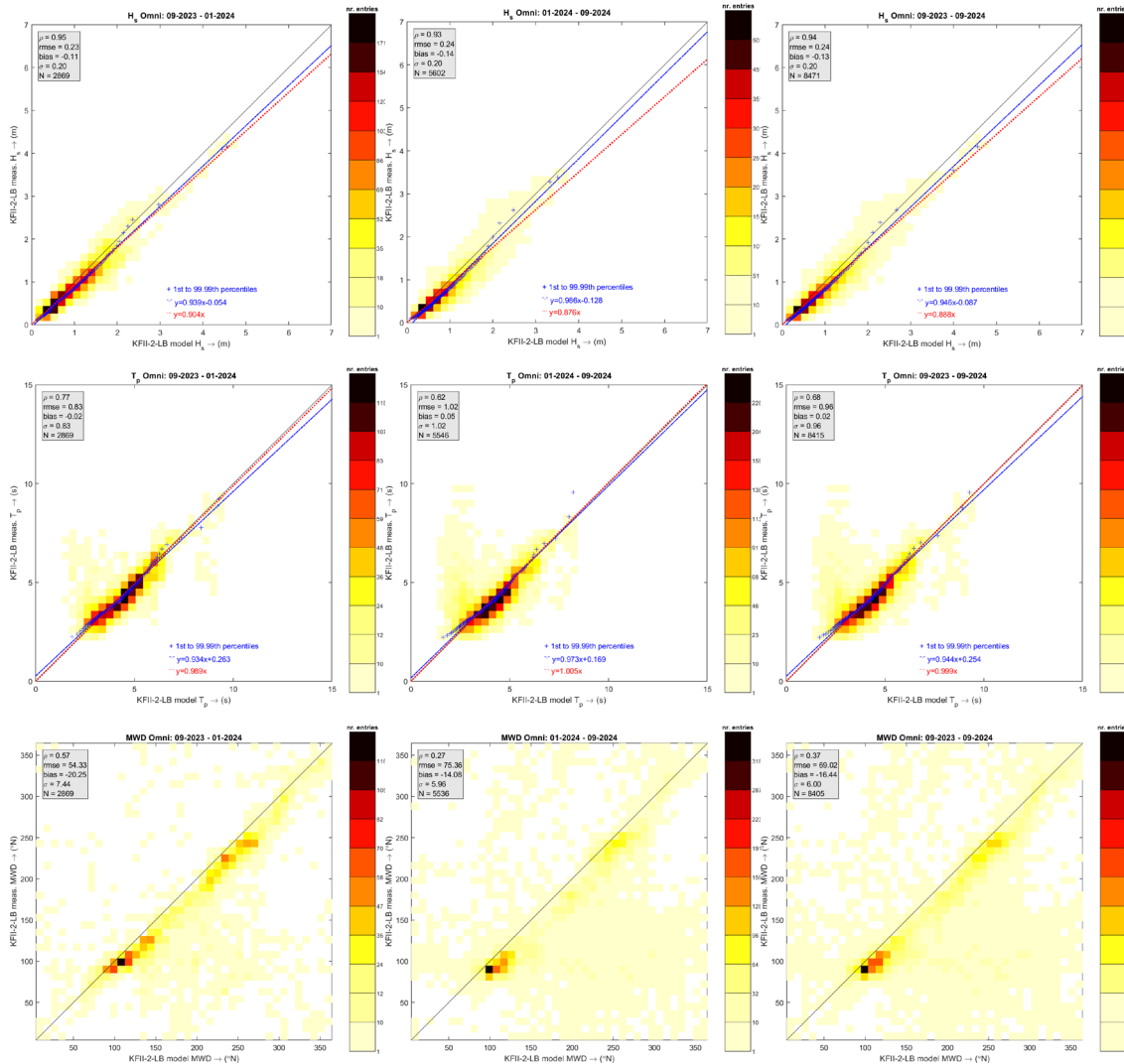


Figure 8-4 Density scatter comparisons between the calibrated model results and the observations from KFII-2-LB of significant wave height (top row), peak wave period (middle row) and mean wave direction (bottom row). The periods covered by the data are 09-2023 to 12-2023 (left column), 01-2024 to 09-2024 (middle column) and 09-2023 to 09-2024 (right column).

8.4 KFII-3 waves

Figure 8-5 shows the timeseries comparisons between the model results and the observations of H_s , T_p and MWD at KFII-3-LB. The respective density scatter comparisons are given Figure 8-6. The KFII-3 data have not been considered in Deltares (2024) as it were not yet available then. The density scatter comparisons are therefore for the full campaign period. The figures show that the agreement between the model results and the observations is high and in line with the comparisons for KFII-1-LB and KFII-2-LB. These extra comparisons confirm the validity of the wave model results.). Based on these, we conclude that quality of the basis wave data is as reported in Deltares (2024) and there is no need for recalibration.

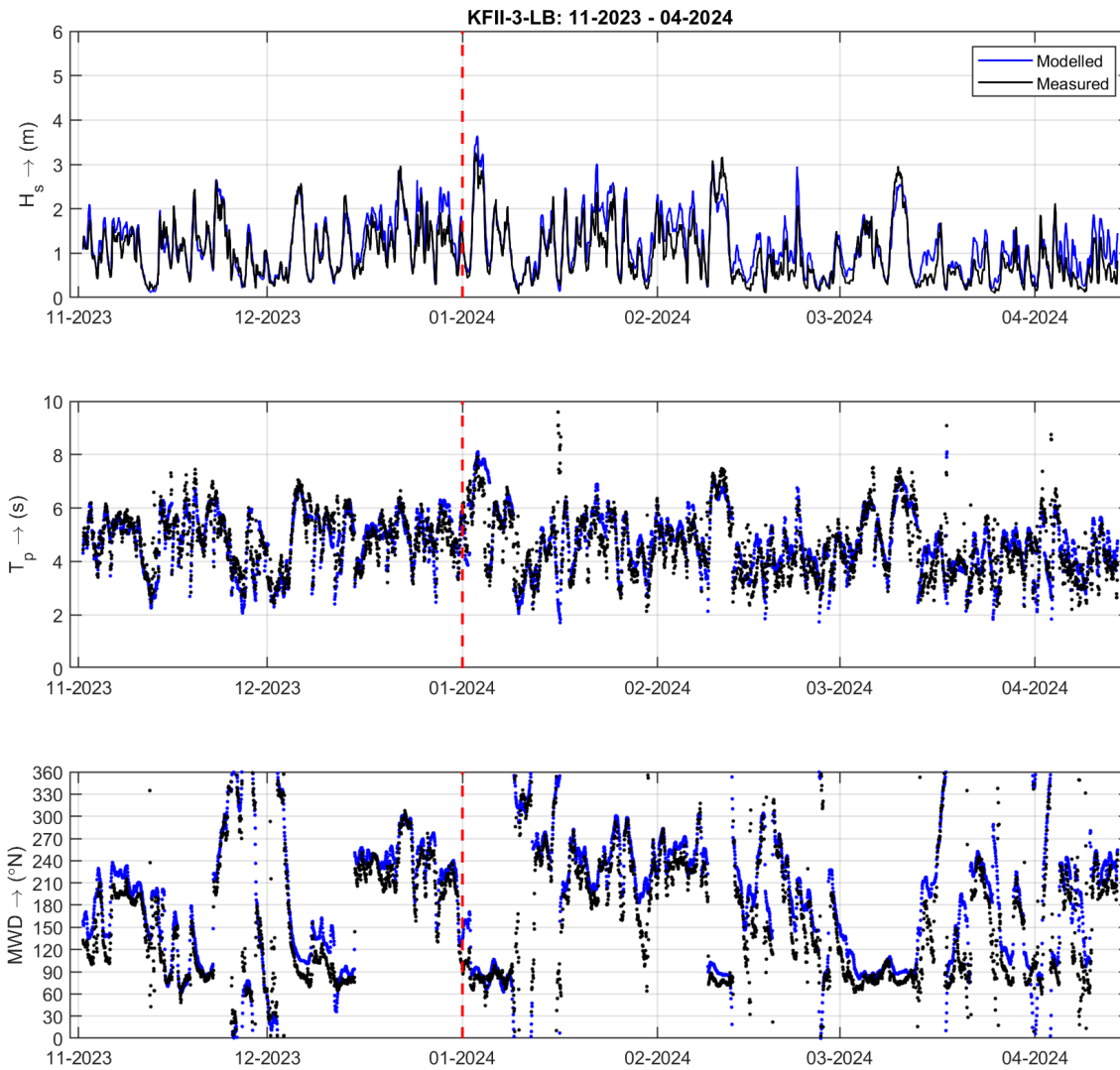


Figure 8-5 Timeseries comparisons between the calibrated model results and the observations from KFII-3-LB of significant wave height (top panel), peak wave period (middle panel) and mean wave direction (bottom panel). The vertical line indicates the end of 2023.

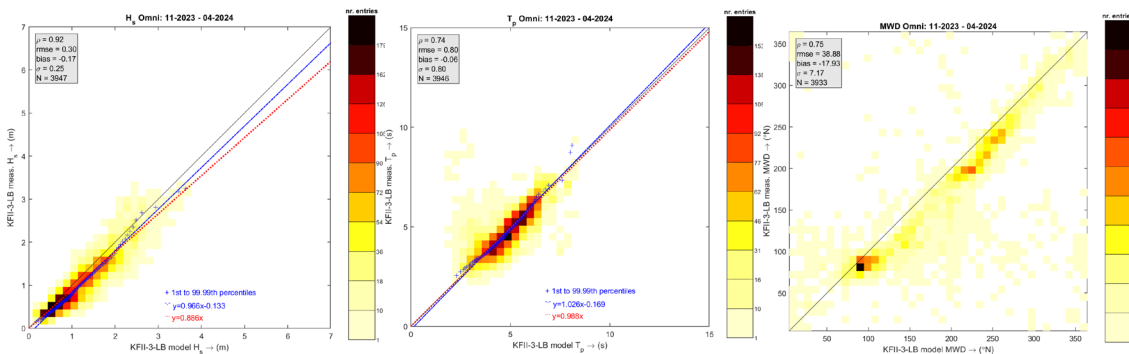


Figure 8-6 Density scatter comparisons between the calibrated model results and the observations from KFII-3-LB of significant wave height (left), peak wave period (middle) and mean wave direction (right).

9 References

- Deltares, 2024: Kriegers Flak II Site Metocean Conditions Assessments, Part A: Measurements and Hindcast Data Basis, dated 15-10-2024 (KFII_Report_PartA_for_ENDK-SWECO_rev3 - signed.pdf).
- Fugro, 2024a: Danish Offshore Wind 2030 – Floating LiDAR Measurements Final Campaign Report for Kriegers Flak II, 3 September 2023 - 3 September 2024, C75517-R12-KFII 01, dated: 4-11-2024 (C75517-R-KFII-M12(01)_12MReport.pdf).
- Fugro, 2024b: Final Report for Kriegers Flak II (KFII-3), 1 November 2023 – 14 April 2024, C75517-R6-KFII3-001 (02), dated: 11-11-2024 (C75517-R6-KFII3-001(02).pdf).
- SWECO, 2024: Kriegers Flak II – North and South Site Metocean Conditions Assessments: Part B: Analyses and Design Parameters (41011329B_KG_PartB_Analyses_and_Design_Parameters).

Appendix A Error statistics

Introduction

A particularity of certain environmental data (e.g. wave data) is that they can be classified into *linear data* (e.g. mean wave period and significant wave height) and *circular data* (e.g. mean wave direction and directional spread), and this distinction must be taken into consideration when carrying out error analysis (Van Os and Caires, 2011). The statistical techniques for dealing with these two types of data are different – circular (or directional) data require a special approach. Basic concepts of statistical analysis of circular data are given in the books of Mardia (1972) and Fisher (1993).

Linear variables

Differences between linear variables are often quantified using the following standard statistics:

- the bias: $\bar{y} - \bar{x}$;
- the root-mean-square error: $RMSE = \sqrt{n^{-1} \sum (y_i - x_i)^2}$;
- the scatter index: $SI = \frac{\sqrt{n^{-1} \sum [(y_i - \bar{y}) - (x_i - \bar{x})]^2}}{\bar{x}}$;
- the correlation coefficient: $\rho = \frac{\sum [(x_i - \bar{x}) - (y_i - \bar{y})]}{\sqrt{\sum (x_i - \bar{x})^2 \sum (y_i - \bar{y})^2}}$;
- the symmetric slope: $r = \sqrt{\sum x_i^2 / \sum y_i^2}$.

In all these formulae x_i usually represents observations (or the dataset which is considered less uncertain or baseline), y_i represents the model results (or the dataset which is considered more uncertain or with a certain deviation from the baseline results) and n the number of observations. In this study, when trying to derive calibration expressions, x_i corresponds to the model results.

Circular variables

If we compute an average of angles as their arithmetic mean, we may find that the result is of little use as a statistical location measure. Consider for instance the case of two angles of 359° and 1°; their arithmetic mean is 180°, when in reality 359° is only two degrees away from 1° and the mid direction between the two is 0°. This phenomenon is typical for circular data and illustrates the need for special definitions of statistical measures in general.

When dealing with circular data, each observation is considered as unit vector, and it requires vector addition rather than ordinary (or scalar) addition to compute the average of angles, the so-called mean direction.

Writing

$$C_n = \sum_{i=1}^n \cos x_i \quad \text{and} \quad S_n = \sum_{i=1}^n \sin x_i, \quad (\text{A.1})$$

the *sample resultant vector* R_n of a sample $x = \{x_i, i = 1, \dots, n\}$ is defined as

$$R_n = \sqrt{C_n^2 + S_n^2},$$

and its *sample mean direction* $\bar{x} \equiv \bar{x}_n$ as the direction of R_n :

$$\bar{x} = \text{TAN}^{-1}(S_n/C_n) \quad (\text{A.2})$$

where $\text{TAN}^{-1}(S_n/C_n)$ is the inverse of the tangent of (S_n/C_n) in the range $[0, 2\pi]$, i.e.,

$$\text{TAN}^{-1}\left(\frac{S_n}{C_n}\right) = \begin{cases} \tan^{-1}\left(\frac{S_n}{C_n}\right), & S_n > 0, C_n > 0 \\ \tan^{-1}\left(\frac{S_n}{C_n}\right) + \pi, & C_n < 0 \\ \tan^{-1}\left(\frac{S_n}{C_n}\right) + 2\pi, & S_n < 0, C_n > 0. \end{cases}$$

The *sample mean resultant length* of $x = \{x_i, i = 1, \dots, n\}$ is defined by

$$\bar{R}_n = R_n/n, 0 < \bar{R}_n < 1$$

If $\bar{R}_n = 1$, then all angles coincide.

Eq. (A.1) can be used to compute the bias between two circular variables by substituting x_i by $y_i - x_i$ in Eq. (A.2). In a similar way, the root-mean-square error and standard deviation between two circular variables can be computed.

Since circular data are concentrated on $[0^\circ, 360^\circ]$, and in spite of the analogies with the linear case, it makes no sense to consider a symmetric slope for circular data other than one.

There are several circular analogues of the correlation coefficient, but the most widely used is the one proposed by Fisher and Lee (1983), the so-called *T-linear correlation coefficient*. Given two sets $x = \{x_i, i = 1, \dots, n\}$, $y = \{y_i, i = 1, \dots, n\}$ of circular data, the *T-linear correlation coefficient* between x and y is defined by

$$\rho_T = \frac{\sum_{1 \leq i < j \leq n} \sin(x_i - x_j) \sin(y_i - y_j)}{\sqrt{\sum_{1 \leq i < j \leq n} \sin^2(x_i - x_j) \sum_{1 \leq i < j \leq n} \sin^2(y_i - y_j)}}.$$

This statistic satisfies $-1 \leq \rho_T \leq 1$, and its population counterpart (which is not given here but can be seen in Fisher and Lee, 1983) satisfies properties analogous to those of the usual population correlation coefficient for linear data: that is, the population counterpart achieves the extreme values -1 and 1 if and only if the two population variables involved are exactly 'T-linear associated', with the sign indicating discordant or concordant rotation, respectively (see Fisher (1993), p. 146, for these concepts).

For computational ease, we use an equivalent formula for ρ_T , given by Fisher (1993):

$$\rho_T = \frac{4(AB-CD)}{\sqrt{(n^2-E^2-F^2)}\sqrt{(n^2-G^2-H^2)}}$$

where

$$A = \sum_{i=1}^n \cos x_i \cos y_i, \quad B = \sum_{i=1}^n \sin x_i \sin y_i,$$

$$C = \sum_{i=1}^n \cos x_i \sin y_i, \quad D = \sum_{i=1}^n \sin x_i \cos y_i,$$

$$E = \sum_{i=1}^n \cos(2x_i), \quad F = \sum_{i=1}^n \sin(2x_i),$$

$$G = \sum_{i=1}^n \cos(2y_i), \quad H = \sum_{i=1}^n \sin(2y_i).$$

References

Fisher, N.I., 1993. Statistical analysis of circular data. Cambridge Univ. Press, 277 pp.

Fisher, N.I. and A.J. Lee, 1983. A correlation coefficient for circular data. Biometrika, 70, pp. 327-32.

Mardia, K.V., 1972. Statistics of directional data. Academic Press, (London and New York).

Van Os, J. and S. Caires, 2011: How to Carry out metocean studies. Proc. 30th Int. Conf. on Offshore Mechanics and Arctic Eng. (OMAE2011-49066).